

New geophysical insight into the origin of the Denali volcanic gap

Stéphane Rondenay,¹ Laurent G. J. Montési² and Geoffrey A. Abers³

¹Department of Earth, Atmospheric and Planetary Sciences, Massachusetts Institute of Technology, Cambridge, MA, USA. E-mail: rondenay@mit.edu

²Department of Geology, University of Maryland, College Park, MD, USA

³Lamont-Doherty Earth Observatory, Columbia University, Palisades, NY, USA

Accepted 2010 May 11. Received 2010 May 11; in original form 2009 December 6

SUMMARY

Volcanic gaps are segments of subduction zones that lack the volcanic activity usually found at these convergent margins. They are regions where the necessary conditions to produce melt may appear favourable, but where volcanoes are surprisingly absent from the surface. In this study, we present a new model that can explain the occurrence of such volcanic gaps. It is based on seismic imaging and geodynamic modelling of the Denali volcanic gap, a ~400-km-wide region at the eastern end of the Alaska-Aleutian subduction zone. Here, the thick crust of the Pacific Plate and Yakutat terrane subduct at shallow angle beneath North America. A high-resolution seismic profile clearly images the subducting crust undergoing progressive dehydration between 50 and 120 km depth, and a negative subhorizontal velocity contrast at 60 km depth in the overlying mantle wedge. We interpret this 60 km discontinuity as marking the top of a layer of partial melt that pools at the base of the overriding plate. In steady-state subduction models, melt accumulates at the apex of a vaulted mantle wedge, the ‘pinch zone’, from where it may break through the overlying lithosphere to the surface. Beneath the Denali volcanic gap, the pinch zone is absent (or greatly reduced) because shallow subduction of the Yakutat terrane progressively cools the system, and causes the slab to advance and replace the hot core of the mantle wedge. This regime can be seen as the opposite of subduction roll-back. It prevents the formation of a pinch zone, reduces the length of the melting column and causes melt to pool at the base of the overriding plate, thus inhibiting magma generation and extraction.

Key words: Wave scattering and diffraction; Subduction zone processes; Volcanic arc processes; Dynamics of lithosphere and mantle.

1 INTRODUCTION

Volcanic arcs are a common feature of subduction zones. Magma in these systems may be produced through hydrous melting (Tatsumi *et al.* 1983), anhydrous decompression melting (Conder *et al.* 2002) or, perhaps in rare cases, direct melting of the subducted slab (Yogodzinski *et al.* 2001). However, there are portions of subduction zones referred to as ‘volcanic gaps’ where volcanism is absent. Some of these gaps occur in regions where the subducted slab lies flat beneath the overriding plate, such as in parts of the Andes (e.g. James & Sacks 1999). Mantle wedge circulation is shut down in this type of regime, causing a cooling of the system and inhibiting melt production (James & Sacks 1999; Kay *et al.* 1999).

There exists another class of subduction environment where volcanism is absent despite seemingly favourable conditions. One such region, the Denali volcanic gap, is found at the eastern end of the Alaska-Aleutian subduction system. Here, the Pacific Plate is subducting at a shallow angle beneath North America, forming a system that is almost inactive volcanically but that is associated with the rapid uplift of North America’s highest mountain ranges. Prior seis-

mic results indicate that the slab is undergoing dehydration in this region (e.g. Rondenay *et al.* 2008) and that the mantle wedge is warm enough to cause partial melting under water-saturated conditions (e.g. Stachnik *et al.* 2004). The objective of this work is to determine the cause of this volcanic gap by interpreting new, high-resolution teleseismic imaging results from the area in conjunction with constraints from geodynamic models.

1.1 Geological setting

The Aleutian-Alaska margin extends over a distance of 2500 km. It is the result of 220 Myr of accretionary and deformational history (Plafker *et al.* 1994) driven by the subduction of the Farallon and Kula plates until 55 Ma followed by that of the Pacific plate. At the eastern end of the Alaska-Aleutian arc, in central Alaska (Fig. 1), the Pacific Plate currently converges with North America at a rate of ~55 mm yr⁻¹ towards the NNW (DeMets *et al.* 1994). The plate is 35–45 Myr in age at the trench (Atwater 1989), placing it in the mid-range of slab thermal structures relative to subduction zones worldwide (Kirby *et al.* 1996). The downgoing slab here can be

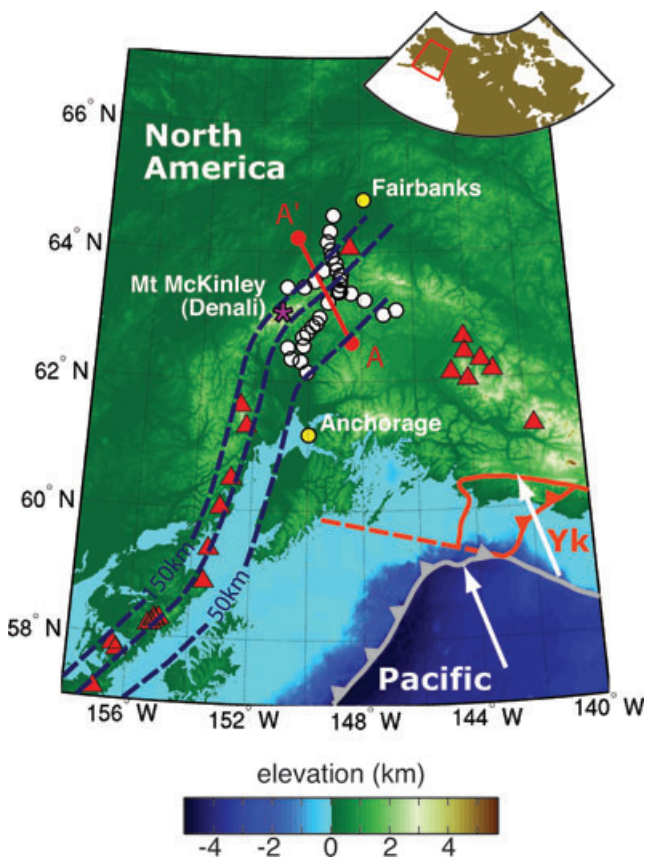


Figure 1. Elevation map of central Alaska. Inset shows the location of the study area relative to North America. Solid grey and orange lines show the surface contacts of the Pacific Plate and Yakutat (Yk) terrane, respectively (Plafker *et al.* 1994; Ferris *et al.* 2003). The rate of convergence between the coupled Pacific-Yakutat and North America is $\sim 55 \text{ mm yr}^{-1}$, in the direction indicated by the white arrows. Toothed lines represent subduction trenches. The dashed orange line marks the southwestern extent of the subducted Yakutat terrane based on aeromagnetic anomaly (Ferris *et al.* 2003). The dashed blue lines are slab depth isocontours based on Wadati-Benioff seismicity (Ratchkovski & Hansen 2002). Red triangles indicate major Quaternary volcanoes. The seismic array, denoted by white circles, is located in the centre of the Denali volcanic gap. The surface projection of the seismic profile (Figs 3–4) is indicated by line A–A’.

divided into the Cook Inlet segment to the west of $\sim 152^\circ \text{W}$, which undergoes fairly typical subduction, and the anomalous Denali segment between ~ 152 and 148°W . The latter is characterized by (i) an overlying plate that is largely inactive volcanically and is therefore referred to as the ‘Denali volcanic gap’ (Nye 1999), (ii) seismicity that extends to only 100–140 km depth in contrast to 150–300 km depth farther to west and (iii) a thrust zone that reaches widths of 350–400 km down dip, creating a system which is sometimes described as flat slab subduction (Gutscher & Peacock 2003). The Wadati-Benioff zone ends east of 148°W , where intermediate-depth seismicity is absent except for a cluster of earthquakes beneath the Wrangell volcanoes (Page *et al.* 1989).

The Denali segment has exhibited low volcanic activity at least since the Miocene. It is 400 km wide along strike and separates the currently active Aleutian arc to the west from the Wrangell volcanoes to the east (Fig. 1). The existence of this gap is poorly understood. Although it is located near the eastern terminus of the subduction front, Wadati-Benioff seismicity (Ratchkovski & Hansen 2002) and velocity anomalies associated with cold descending lithosphere

(Zhao *et al.* 1995; Eberhart-Phillips *et al.* 2006) clearly indicate that a continuous, dipping oceanic slab is currently subducting beneath most of the region. However, the volcanism usually associated with subduction is absent except for one suite of small-volume cinder cones at the eastern end of this segment, the 3000-year-old Buzzard Creek Maars, whose composition indicates a subduction affinity (Nye 1999). Thus, melts are present in the mantle beneath the Alaska range but rarely reach the surface.

The volcanic gap is likely linked to the unique tectonic setting of central Alaska, which involves the shallow subduction of the buoyant Yakutat terrane and a resulting compressive stress regime in the upper plate (e.g. Pavlis *et al.* 2004; Abers 2008; Gulick *et al.* 2007). The Yakutat block is a composite terrane partially coupled to the Pacific Plate that comprises an abnormally thick or tectonically doubled, buoyant oceanic crust (Plafker *et al.* 1994). Portions of this terrane that have subducted completely beneath the Aleutian megathrust are imaged by refraction as a 15–20 km thick subhorizontal layer beneath coastal Alaska (Brocher *et al.* 1994). Receiver function (RF) analyses suggest that this thick crustal layer extends to depths of 100–140 km some 600 km inland from the trench, perhaps the best example of ongoing subduction of thick crust (Ferris *et al.* 2003; Rossi *et al.* 2006; Rondenay *et al.* 2008).

Numerical models and statistical compilations of subduction zone parameters have shown that shallow subduction is often associated with an advancing trench and upper-plate compression, with the latter causing crustal thickening and mountain building in the arc region (e.g. Arcay *et al.* 2008; Lallemand *et al.* 2005). In central Alaska, the shallow subduction of the Yakutat terrane has been linked to the formation of the Chugach-St. Elias range (Plafker *et al.* 1994; Pavlis *et al.* 2004; Gulick *et al.* 2007). The age of Chugach-St. Elias deformation, in conjunction with the imaged length of Yakutat terrane subducted to date, thus places the onset of Yakutat subduction at 10–12 Ma (Pavlis *et al.* 2004; Gulick *et al.* 2007). Rapid exhumation of the Denali Massif in the Alaska Range, starting at ~ 5.6 Ma, is perhaps another consequence of Yakutat subduction (e.g. Abers 2008), although it has also been attributed to a rapid change in relative motion between the Pacific and North American plates (Fitzgerald *et al.* 1995).

1.2 Geophysical constraints

Over the past decades, a large number of geophysical investigations have provided insight into the structure and dynamics of the southern Alaska subduction system. Here, we summarize those results that have bearing on our understanding of the mantle wedge.

At the top of the system, the continental crust has a variable thickness that is related to the variable nature of its constitutive blocks and ongoing deformation. Receiver function analyses suggest that crustal thickness varies between ~ 26 and 45 km (Rossi *et al.* 2006; Veenstra *et al.* 2006). These fluctuations generally reflect isostatic compensation of topography in the Alaska Range, provided some changes in crustal density associated with the different terranes that make up southern Alaska (Veenstra *et al.* 2006).

At the base of the system, the subducted slab is seismically detected to depths >150 km (Zhao *et al.* 1995; Ratchkovski & Hansen 2002; Eberhart-Phillips *et al.* 2006). Tomographic images exhibit the slab as a high-velocity, dipping layer with a thickness of 30–60 km and seismic velocities that are 3–6 per cent higher than the surrounding mantle (Zhao *et al.* 1995; Eberhart-Phillips *et al.* 2006). The slab dips shallowly ($<10^\circ$ with possibly some flat segments; Brocher *et al.* 1994) from the trench to at least 350 km

landward of the trench, after which it plunges at $\sim 22^\circ$ (Ferris *et al.* 2003). This dipping angle at depth is $2\text{--}4^\circ$ smaller than that suggested by Wadati-Benioff seismicity, indicating that seismicity may not outline a horizon parallel to the subduction interface but rather one that plunges more steeply into the slab, following a positive P-T slope (Abers *et al.* 2006).

Sandwiched between the continental crust and the subducted slab, the mantle wedge can be partitioned into several domains based on seismic properties and geodynamic constraints. First, in the region of the wedge where the slab surface is ≤ 80 km depth, low-seismic attenuation (high- Q) indicates that this portion of the system has a high viscosity and is therefore isolated from the corner flow (Stachnik *et al.* 2004; Abers *et al.* 2006). This is in agreement with the observations of Blakely *et al.* (2005), who attribute a strike-parallel band of high aeromagnetic anomaly coupled with a low Bouguer anomaly to a serpentinized mantle wedge in the region where the subduction interface is $\leq 50\text{--}75$ km depth. Similar models were proposed for other subduction zones on the basis of thermal models showing that serpentine stability conditions (i.e. $< 600\text{--}700^\circ$ for antigorite at these depths) may be encountered in the cold nose of a mantle wedge (Hyndman & Peacock 2003). Second, downdip of the slab's 80 km depth contour, high attenuation suggests a transition to the warmer, circulating portion of the mantle wedge (Stachnik *et al.* 2004). The inferred temperature in the wedge there is $\sim 1250^\circ\text{C}$, below the dry solidus for peridotite of 1420°C at 2.45 GPa (Hirschmann 2000) but hot enough to allow some wet melting. This distribution of Q is similar to that observed in other subduction systems such as NE Japan that do possess an active volcanic arc. Third, in a portion of the mantle wedge that likely straddles the two regions described above, receiver functions detect unusually low V_p/V_s ratio values (< 1.70) interpreted as due to underthrust siliceous crustal material in the mantle beneath central Alaska (Rossi *et al.* 2006).

2 SEISMIC IMAGING: METHOD AND DATA

2.1 Methodology

To produce high-resolution seismic images of the subsurface, we use a teleseismic migration approach based on multichannel inversion of scattered body waves recorded at dense recording arrays (Bostock *et al.* 2001; Rondenay *et al.* 2005). The problem is posed for forward- and backscattered wavefields generated at discontinuities in a 2-D isotropic medium, with the backprojection operator cast as a Generalized Radon Transform (GRT). The approach allows for the treatment of incident plane waves from arbitrary backazimuths, and recovers estimates of material property perturbations (e.g. S and P velocity) about a smoothly varying reference model. In the rest of the text, the method is referred to as the 2-D GRT inversion.

In theory, the 2-D GRT inversion allows for simultaneous treatment of seven independent scattering modes: two forward modes ($q_1 = P_d\dot{p}$, $q_2 = P_d\dot{s}$) and five backscattered modes associated with free-surface reverberations of the incident wave ($q_3 = P\dot{p}_d\dot{p}$, $q_4 = P\dot{p}_d\dot{s}$, $q_5 = P\dot{s}_d\dot{p}$, $q_6 = P\dot{s}_d\dot{s}|_v$, $q_7 = P\dot{s}_d\dot{s}|_h$). q_n indicates the mode number with $n = 1\text{--}7$, P is the upgoing incident wave, \dot{p} and \dot{s} are downgoing waves reflected off the free-surface, subscript d denoted the scatterer, \dot{p} and \dot{s} are upgoing scattered waves, and v and h indicate vertical and horizontal shear-wave polarization, respectively. However, due to inexact isolation of the

scattered wavefield during data pre-processing and weak reflection/transmission coefficients of waves that undergo multiple conversions (e.g. P -to- S and S -to- P , as in q_5), only modes $n = 2, 3, 4, 6, 7$ are well recovered in practice (Bostock *et al.* 2001; Rondenay *et al.* 2005).

The 2-D GRT inversion operates on the scattered wavefield of the P coda, and therefore the raw data must undergo a fair amount of preconditioning prior to being input into the imaging algorithm. The main pre-processing steps are: (1) rotation of the data into radial, transverse and vertical (R, T, Z) components; (2) removal of the free-surface effects and projection of the wavefield into P, SV, SH polarization directions with the free-surface transfer matrix; (3) alignment of the traces relative to the incident P -wave by multichannel cross-correlation; (4) estimation of the incident P -wavelet by eigenimage decomposition; (5) construction of a source-normalized scattered wavefield by subtracting the P -wavelet from the P wavefield and deconvolving the P -wavelet from the resulting P' , SV and SH wavefields and (6) rotating the estimated scattered wavefields into the Cartesian axis system imposed by the 2-D geometry of the target structure and applying filters that arise from the analytical formulation of the 2-D GRT. The resulting waveforms are bandpass filtered using a 2-pass (zero-phase) Butterworth filter with cut-offs at 0.3–0.03 Hz, to remove the effects of scattering from surface topography. A full description of these pre-processing steps is given in Bostock & Rondenay (1999) and Rondenay *et al.* (2005).

2.2 Seismic experiment and dataset

We analyse data recorded in southern Alaska by the Broadband Experiment across the Alaska Range (BEAAR), an array consisting of 36 portable broadband seismometers deployed in 1999–2001, for a period of 2.5 yr (Ferris *et al.* 2003). The design of the experiment was strongly influenced by the road system, with most of the array following the Parks Highway that joins Fairbanks to Anchorage.

Since the 2-D GRT inversion has stringent data requirements (see Rondenay *et al.* 2005), waveforms from only 23 events recorded by the BEAAR array could be used in the analysis. Waveforms were selected based on their high signal-to-noise ratio and the stability of their deconvolution by the estimated source wavelet. This selection strategy is necessary because noise and oscillations due to spectral division tend to sum constructively in the final image and cause structural artefacts (see Rondenay *et al.* 2005). The distribution of the selected events is shown in Fig. 2, along with a typical data section. Backazimuthal coverage, although not comprehensive, ensures illumination of the subducted slab from updip and downdip directions.

The relative traveltimes of incident and scattered waves are calculated for an average 1-D background model based on the results of (Rossi *et al.* 2006), with a crust of 36.2 km thickness ($V_p = 6.5 \text{ km s}^{-1}$, $V_p/V_s = 1.78$) over a half-space ($V_p = 7.81 \text{ km s}^{-1}$, $V_p/V_s = 1.73$).

3 HIGH-RESOLUTION SEISMIC PROFILES

3.1 Principal observations

The results of the migration are shown in Figs 3 and 4. Fig. 3 shows the contribution of each scattering mode, whereas Fig. 4 shows the resulting model for multimode inverse scattering. These profiles display perturbations in either P - or S velocity, with red to blue

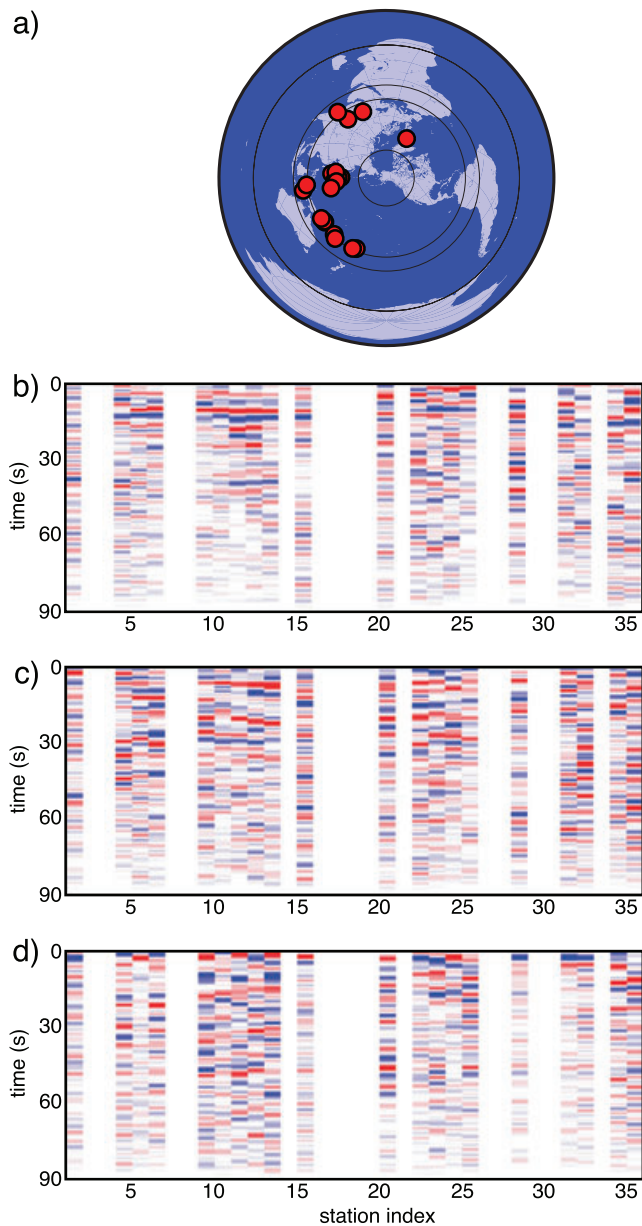


Figure 2. (a) Distribution of the 23 events used for 2-D GRT inversion relative to the study area (centre of the map). (b–d) Typical pre-processed data sections used for analysis, in this case for a magnitude 6.3 mb event from Ryukyu Islands, Japan (2000/06/06). Each vertical column represents one pre-processed seismogram, for stations numbered in increasing order from SE to NW, or A to A', along the projection line shown in Fig. 1. The pre-processed seismograms are colour coded such that red/blue denote positive/negative pulses. Data sections are shown for (b) the x_1 -axis, which is horizontal and parallel to line A–A' in Fig. 1, (c) the x_2 -axis, which is horizontal and perpendicular to line A–A' in Fig. 1, and (d) the x_3 -axis, which is vertical.

colour scale representing negative (slower) to positive (faster) velocity perturbations. In this type of profile, velocity discontinuities are thus denoted by colour contrasts (i.e. red-to-blue or blue-to-red). As in previous applications of this migration approach, we will focus our interpretation on the S velocity (dV_S/V_S) profile, as dV_S/V_S images have been shown to be more robust than the dV_P/V_P images (Rondenay *et al.* 2001, 2005; Rondenay 2009). There are two main reasons for the superiority of dV_S/V_S images. First, they are based

on a larger number of scattered waves that afford superior volume and dip resolution. Second, they are based on S -scattered waves that are more accurately separated from the full recorded wavefield than P waves—something that is especially true for signals scattered at horizontal discontinuities. Thus, we show the dV_P/V_P profile for completeness, but the limited resolution it affords precludes a meaningful $d\ln V_S/d\ln V_P$ analysis and we concentrate our discussion on the dV_S/V_S profile.

Based on previous results from the same method applied in subduction zone settings, a preliminary assessment of the dV_S/V_S image indicates the presence of three main features: (1) a subhorizontal discontinuity with a positive velocity gradient (slow-to-fast downward) extending across most of the profile at an average depth of 40 km, which corresponds to the continental Moho (Veenstra *et al.* 2006; Rossi *et al.* 2006); (2) a dipping low-velocity layer in the SE portion of the array, which correspond to the crust of the subducted slab (see, e.g. Rondenay *et al.* 2008) and (3) a negative velocity gradient at 60 km depth beneath the NW portion of the array. Before interpreting these results in the context of subduction dynamics and water transport, we verify their robustness.

3.2 Image resolution and robustness

The applicability of the 2-D GRT inversion, the resolution it affords, and the robustness of the resulting images have been discussed in general terms in several publications (Bostock *et al.* 2001; Rondenay *et al.* 2001, 2005; Shragge *et al.* 2001). However, the assessment of these properties in specific field applications is highly dependent on the nature of the main imaging targets and on the field conditions specific to a given experiment. It is therefore important to reassess the capabilities and limitations of the methodology in each field application. In this sections, we investigate the validity of the assumptions made by the 2-D GRT inversion algorithm, and we determine the robustness of the two main features of interest in the image—the dipping low-velocity layer and the 60 km lithospheric discontinuity.

The 2-D GRT inversion relies on a series of simplifying assumptions about the geometry of subsurface structure. In particular, it assumes that scatterers are 2-D (i.e. linear) structures in an otherwise 1-D isotropic background medium. Although most earth structures are 3-D, some first order features such as the Moho and subducted slabs often display a 1-D or 2-D geometry at regional scale. However, two limiting factors are found in southern Alaska: first, the geometry of the subduction zone is not perfectly known and varies along strike; second, the seismic array does not form a perfect line, as station locations were constrained by limited road access. It is therefore important to determine the 2-D regional strike and test the validity of the 2-D assumption to ensure that the main features observed in the final image are not related to mismapping of, or artefacts due to, anisotropy and out-of-plane structure.

We first determine the strike of the main imaging target – in this case the subducted slab. This is achieved by projecting the stations on a series of straight lines of varying azimuths passing through the centre of the array (Fig. 5). The optimal projection line is determined when the following two conditions are met: (i) the dip of the slab is at a maximum, (ii) the thickness of the low-velocity layer is at a minimum. These two conditions are met for an azimuth of $N150E \pm 10^\circ$, yielding a 2-D strike of $N120W$ for the subducted slab. This strike is consistent with that obtained by previous investigators using only intraslab seismicity (Ratchkovski & Hansen 2002; Stachnik *et al.* 2004). For the purpose of this

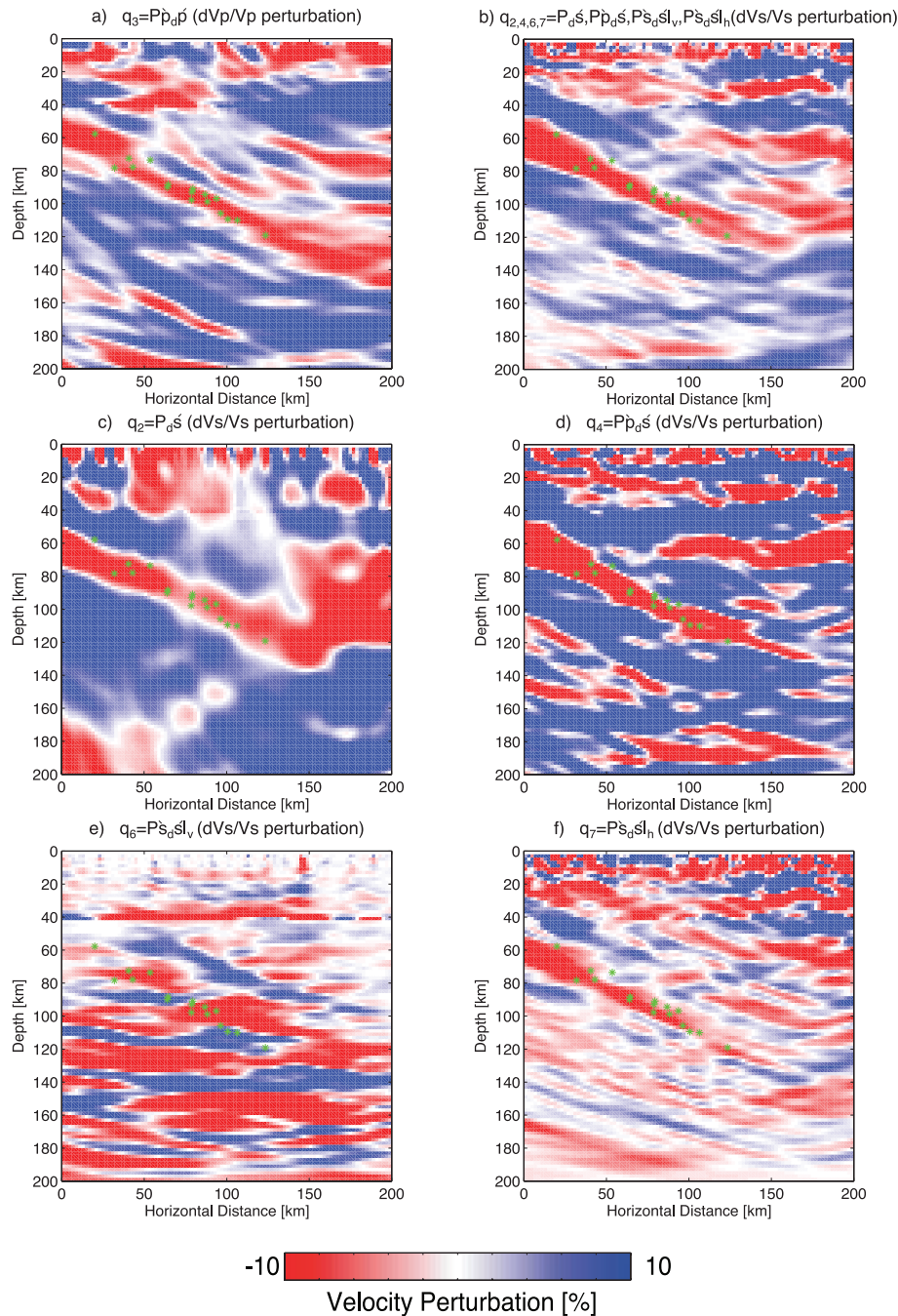


Figure 3. Combined and individual contributions from useful scattering modes, using all the events shown in Fig. 2. (a) dVp/Vp resulting image obtained through mode q_3 , the only mode sensitive to Vp perturbations. (b) dVs/Vs resulting image obtained by combination of modes $q_{2,4,6,7}$, which are the modes sensitive to Vs perturbations. (c–f) dVs/Vs images obtained from individual scattering modes q_2, q_4, q_6, q_7 . Note that the subducted oceanic crust (dipping low-velocity layer), the continental Moho (continuous subhorizontal discontinuity at 30–40 km depth), and the 60 km discontinuity (in the NW portion of the profile) are detected in each individual mode. The resolution is poorest for mode q_6 because most incident waves illuminate the dipping slab obliquely, thus producing stronger SH than SV scattering.

study, mapping of intraslab seismicity can provide an additional constraint on the 2-D strike, as these events are expected to be contained mainly within the subducted crust (see, e.g. Hacker *et al.* 2003). In Fig. 5, we map 18 intraslab events that occurred within 50 km of the BEAAR array during the deployment. Once again, we find that the events are contained within the low-velocity layer only for the azimuth N150E, further supporting a regional 2-D strike of N120W. Therefore, we use this strike to determine the projection

line of the profiles discussed in the remainder of the paper (Figs 3 and 4).

The validity of the 2-D assumption is assessed using both analytical and experimental means. Analytically, the geometrical requirements are validated by ensuring that two-dimensionality is preserved within a region defined by the maximum lateral offset (perpendicular to the projection line) from where detectable scattered signal may occur. It can be shown that for a target at 120 km

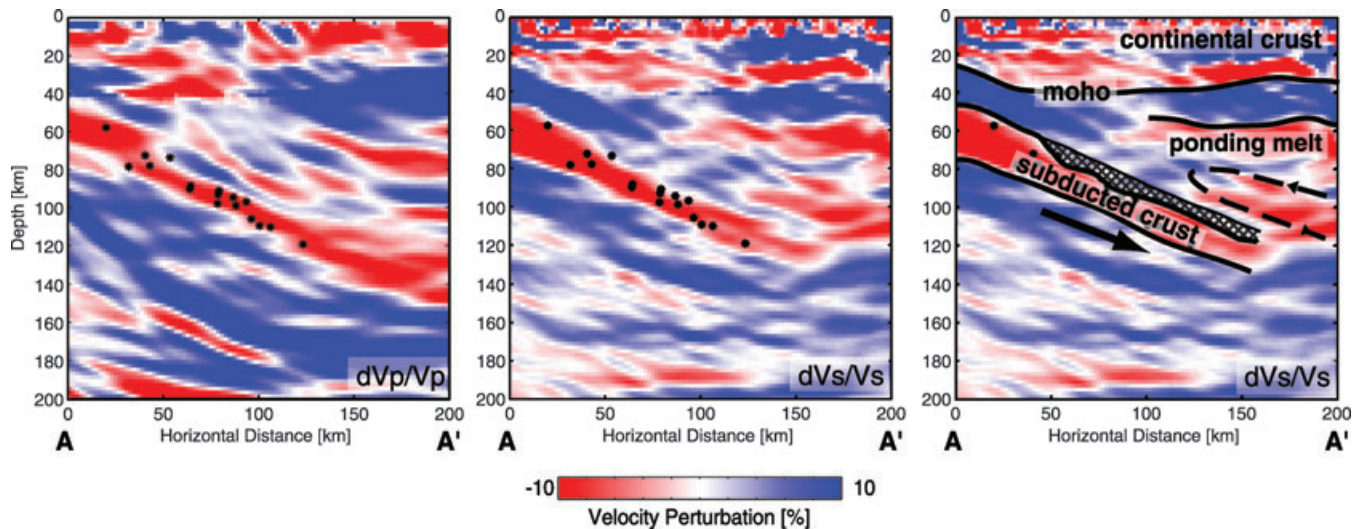


Figure 4. Final V_p and V_s images along profile A–A' (Fig. 1) beneath central Alaska, and V_s image interpretation. Left-hand panel: profile of P -wave velocity perturbation relative to a 1-D layered medium. Middle panel: profile of S -wave velocity perturbation relative to a 1-D layered medium. Discontinuities appear as rapid changes in perturbation polarity, where an increase (decrease) in velocity with depth is referred to as a positive (negative) gradient. Relocated intraslab earthquakes that have occurred within 50 km lateral offset from line A–A' during the deployment period are shown as black stars (Ferris *et al.* 2003). Right-hand panel: interpreted profile. Solid black lines indicate robust discontinuities. The solid arrow denotes the subduction direction and the dashed lines indicate the expected corner flow in the mantle wedge. The crosshatched region represents the subducted crust's upper layer inferred to undergo progressive dehydration-eclogitization with depth (see Section 3.3, and Rondenay *et al.* 2008).

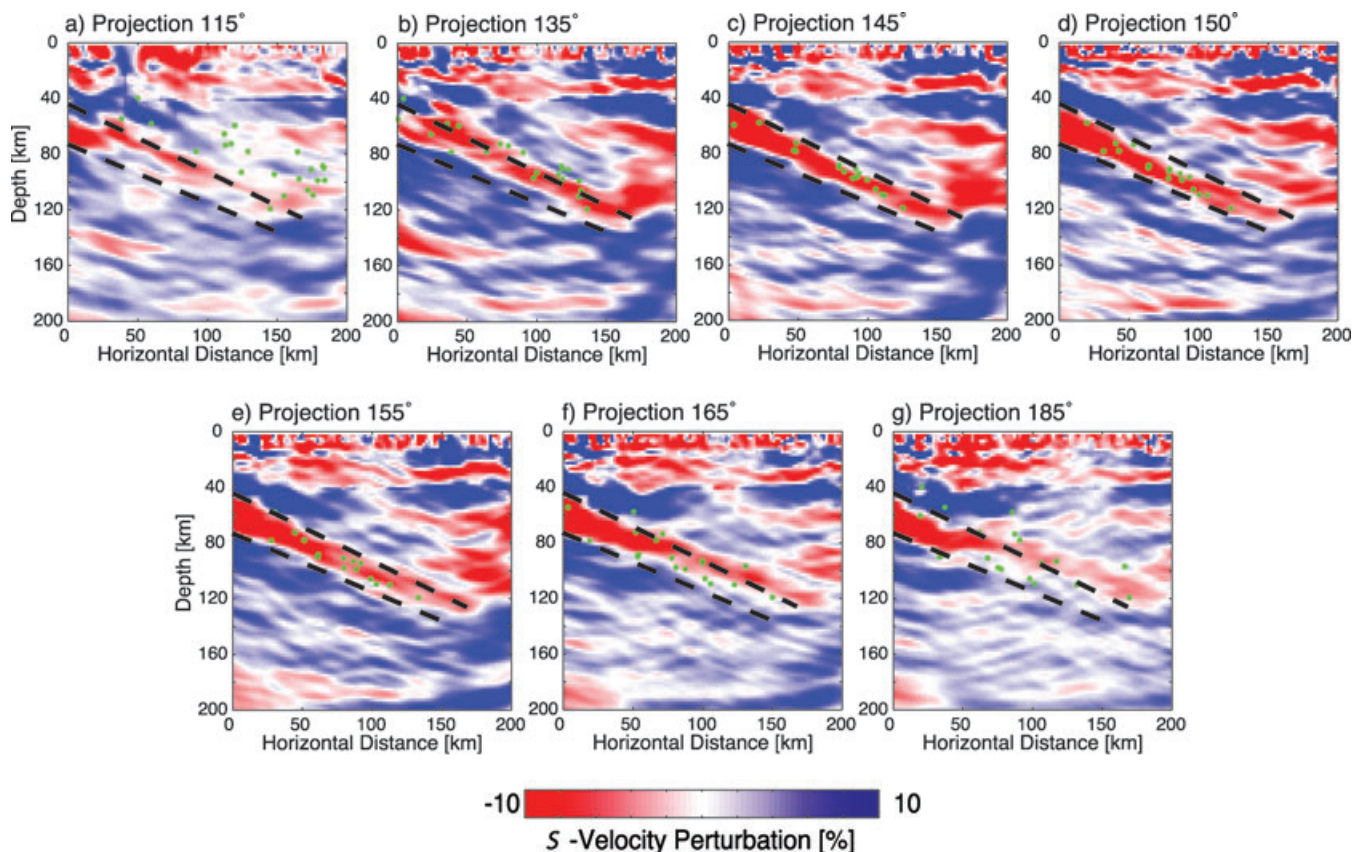


Figure 5. Determination of the 2-D regional strike. Stations are projected on a series of straight lines of varying azimuths passing through the centre of the array, teleseismic data are projected and rotated accordingly, and the migration operator is applied. The optimal projection line is determined when the following two conditions are met: (i) the dip of the slab is at a maximum, (ii) the thickness of the low-velocity layer is at a minimum. These two conditions are met for an azimuth of $N150E \pm 10$ (panel d), where the average dip is 25° and the thickness varies between 20 and 12 km. This yields a 2-D strike of $N120W$ for the subducted slab. Black dashed lines provide the general outline and dip of the low-velocity layer at azimuth $N150E$, and is reproduced at other azimuths for comparison. Green stars indicate local intraslab seismicity within 50 km of the BEAAR array. Note that most events fall within the low-velocity layer at the preferred azimuth.

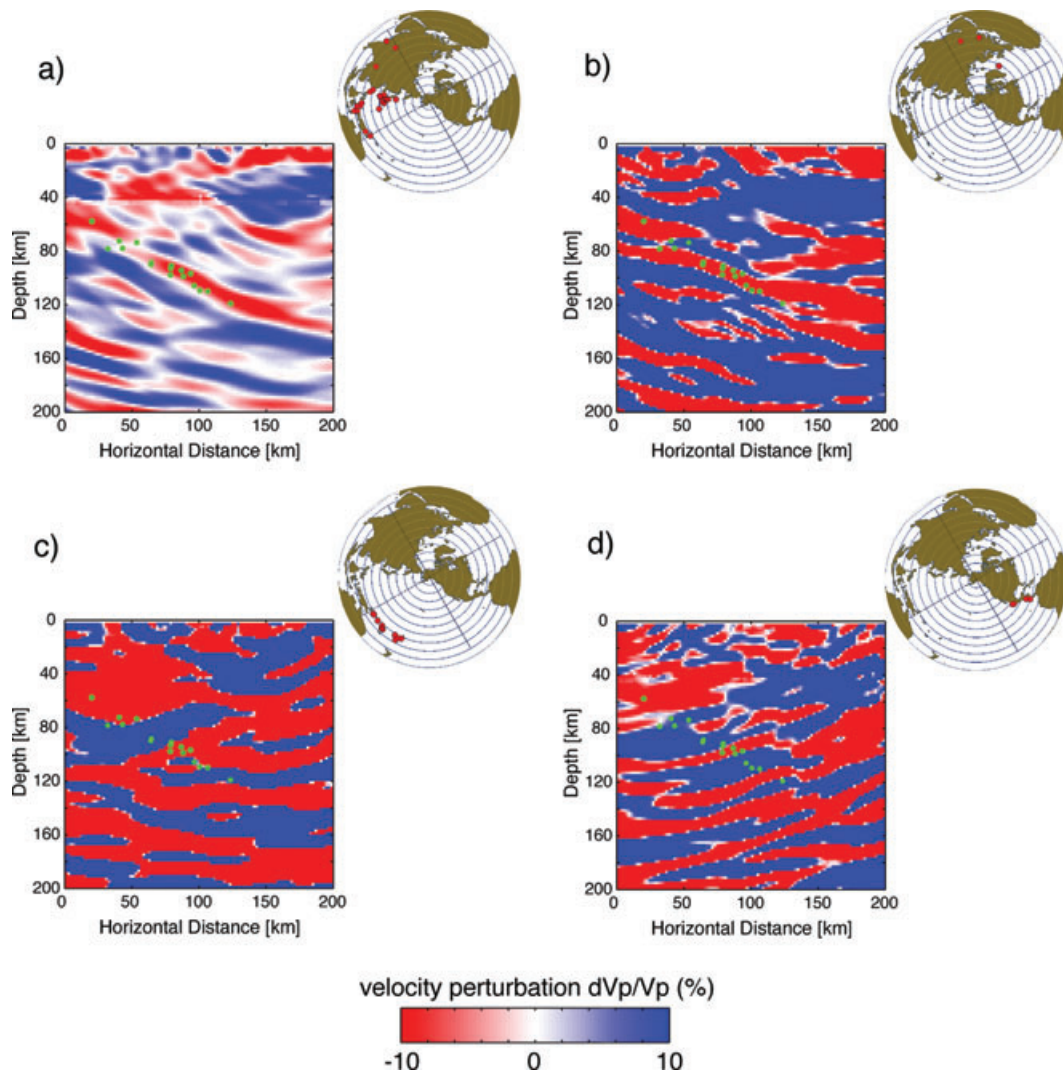


Figure 6. Azimuthal contributions to the dV_p/V_p images. Quadrants and event locations are shown in inset. Quadrants are defined relative to the azimuth of maximum slab dip: (a) quadrant 4, (b) quadrant 1, (c) quadrant 3 and (d) quadrant 2. Note that structure is better resolved by incident waves coming from quadrants 1 and 4 (a–b). This is due to higher transmission and reflection coefficients of P waves across the dipping layer at these azimuths.

depth, the minimum lateral offset on either sides of the station array is of the order of 75 km (Rondenay *et al.* 2005). Based on the slab depth contours shown in Fig. 1, we note that the slab does extend linearly over such distance. Therefore, we can assume that the slab is a 2-D structure beneath our study area. Experimentally, the validation is done by comparing the responses from different event and station subsets. In this case, we verify that the structures imaged in Figs 3 and 4 are observed everywhere beneath the array, for every possible azimuth of illumination. Figs 6 and 7 show that the Moho, the subducted slab and the 60 km discontinuity are robust features that appear to be laterally continuous along a SW-NE 2-D strike.

3.3 Continental Moho

The continental Moho is most clearly observed across the dV_s/V_s profiles of Fig. 4, with a depth fluctuating smoothly between 25 km beneath the SE end of the profile, to a maximum of 42 km beneath the Alaska Range ($x = 70$ km) and back to 32 km in the NW portion of the profile ($x = 175$ km). These depth variations

are generally consistent with previous results and reflect isostatic compensation of the surface topography (Ferris *et al.* 2003; Ai *et al.* 2005; Rossi *et al.* 2006; Veenstra *et al.* 2006; Fuis *et al.* 2008). However, we note that the smooth Moho topography, which is similar to that observed in RF profiles (e.g. Ferris *et al.* 2003), contrasts with the sharp Moho topography suggested by RF analyses conducted at individual stations (Ai *et al.* 2005; Rossi *et al.* 2006; Veenstra *et al.* 2006). Moreover, individual station analyses suggest minimum Moho depths of ~ 26 km in the NW portion of the profile (e.g. Veenstra *et al.* 2006), in contrast with ~ 32 km for RF profiles (e.g. Ferris *et al.* 2003). These discrepancies in Moho topography and depth are most likely due to the fact that profiles are constructed using a 1-D layered reference velocity model, whereas individual station analyses take into account rapid lateral changes in velocity. In particular, lateral variations in V_p/V_s ratio can translate into important fluctuations in discontinuity depth for a constant $S-P$ wave traveltime delay; that is, for a given delay, the discontinuity depth will decrease for increasing V_p/V_s ratio, and vice versa. In Alaska, individual station analyses suggest such rapid interstation variations in V_p/V_s (Rossi *et al.* 2006), whereas the

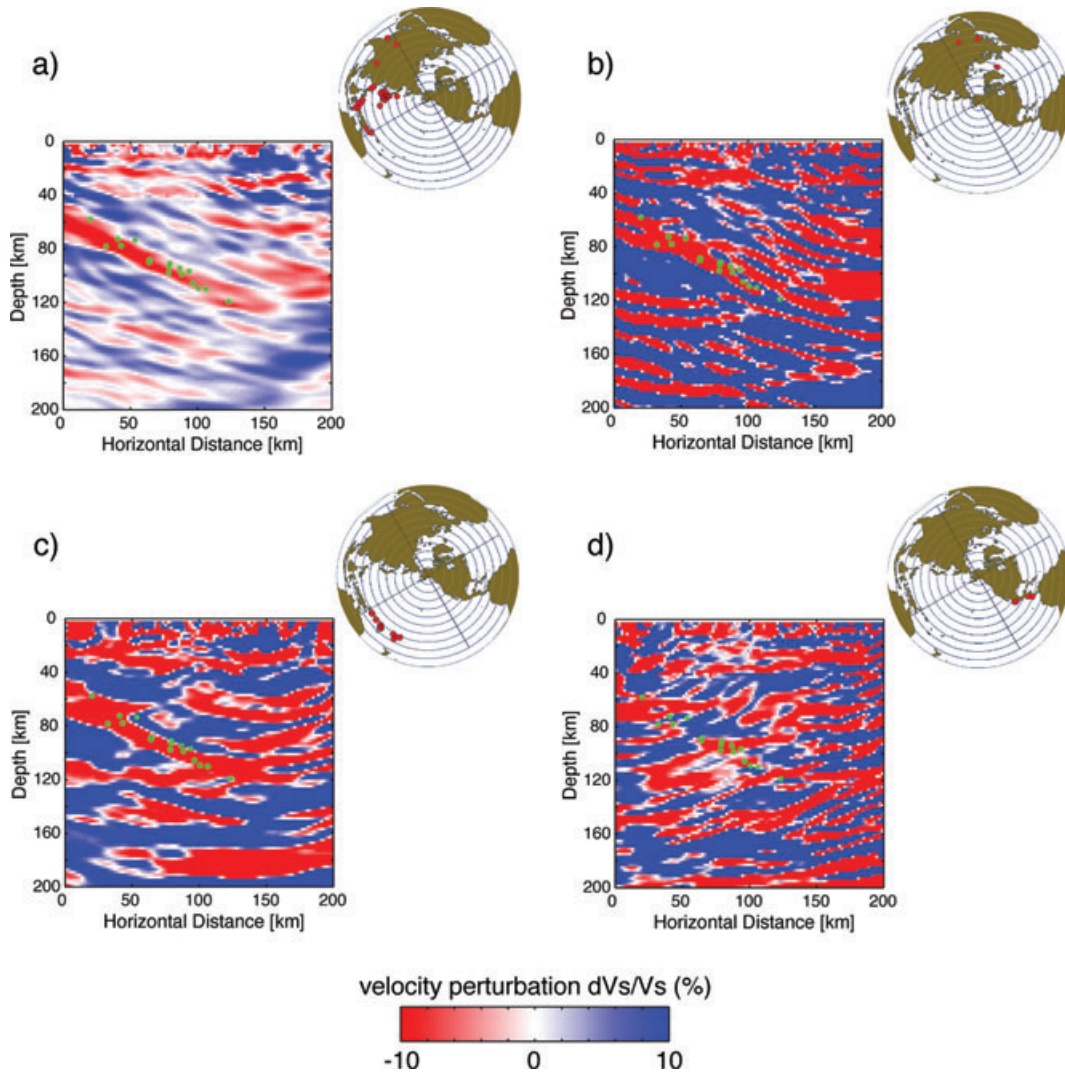


Figure 7. Azimuthal contributions to the dV_s/V_s images. Quadrants and event locations are shown in inset. Quadrants are defined relative to the azimuth of maximum slab dip: (a) quadrant 4, (b) quadrant 1, (c) quadrant 3 and (d) quadrant 2. Note that the main structures (Moho, dipping low-velocity layer, and 60 km discontinuity) are consistently observed when illuminated from all azimuth. Resolution is weaker for quadrant 2 (d) due to the small number of event.

profiles (including the migrated image) are constructed with a average crustal and mantle V_p/V_s ratio, which explains the smoother Moho topography.

Since the current implementation of the teleseismic migration does not support laterally variable background velocities, it is useful to quantify the effects of this simplification on the depth of imaged structure. Here, we estimate the maximum uncertainty on the absolute depth of discontinuities by remapping converted signals for extreme values of V_p/V_s ratios obtained through single-station analyses. For example, with V_p/V_s ratios between 1.62–1.95 in the crust (average 1.78) and 1.61–1.89 in the upper mantle (average 1.73), taken from the results of Rossi *et al.* (2006) beneath the profile, we find a maximum uncertainty of approximately ± 7 km on the absolute depth of the Moho and ± 11 km on discontinuities at 60 km depth for forward scattered waves. These uncertainties are cut by more than half their value for back-scattered waves, which are the main waves contributing to the final image (see, e.g. Rondenay *et al.* 2001). Moreover, one should bear in mind that the actual depth uncertainties are likely much smaller than those quoted above since the extreme values of V_p/V_s used to compute them are

not continuous over the effective recording aperture of the scattered signals used for imaging.

3.4 Dipping low-velocity layer

A tapering of the dipping, low-velocity layer is observed for waves illuminating the study area from all available azimuths. This tapering is unlikely to be an artefact caused by lateral variations in V_p/V_s ratio, since this would cause a similar vertical shift of both the upper and lower boundaries of the low-velocity layer, which is not observed here. Thus it appears to be a robust feature. However, previous analyses showed that the layer thickness remained constant at ~ 20 km from 50 to 120 km depth (Ferris *et al.* 2003). Rondenay *et al.* (2008) showed that previous and new results may be reconciled by taking into account the increase in resolution afforded by the inclusion of backscattered waves in the 2-D GRT inversion. Their findings support a model where the low-velocity layer comprises two sublayers: a top layer containing a velocity gradient occurring over 10 km, that is likely indicative of progressive

dehydration with depth (see crosshatched region in Fig. 4); and a lower layer displaying more uniform low-velocity.

3.5 Lithospheric discontinuity

Between the continental Moho and subducting crust, the mantle wedge exhibits strong coherent layering. The most prominent feature is a low-velocity region marked by a sharp upper boundary at 55–60 km depth (Fig. 4). The boundary represents a negative velocity contrast (i.e. downward fast-to-slow, or blue-to-red, transition). It is strongest at the northern end of the profile, with a magnitude of ~10–13 per cent for S velocities (range based on modelling and comparison to a 15–20 per cent Moho; the P -velocity image exhibits a similar contrast, but is inherently less robust; see, e.g. Rondenay *et al.* 2005), and becomes indistinct in the region where the depth of the subduction interface is less than 80–100 km. Here, we test the robustness of the 60 km discontinuity to ensure that the signal is not related to a free-surface multiple or a processing artefact. Then we put some bounds on the properties of this low-velocity layer.

Individual 1-D receiver functions are computed for single stations in the NW portion of the array, where the discontinuity is

observed, and they are then modelled using a synthetic reflectivity approach. Figs 8–10 present the results from this exercise for station NNA, the northernmost station of the array. The receiver functions obtained at station NNA are shown in Fig. 8, migrated at 1-D phasing depths (i.e. conversion or reflection depths) corresponding to relevant forward and backscattered modes. These are stacked waveforms from seven events with NW and SE azimuths. The Moho and 60 km discontinuity appear at different depths in the various modes due to inaccuracies in the 1-D depth-migration operator. Synthetics in Fig. 9 show that a single Moho discontinuity cannot explain the occurrence of the 60 km phase, whereas those in Fig. 10 show that a real velocity drop at 60 km depth is required to produce a phase that is systematically observed by all the modes at that depth. Note that $P\delta_d\delta|_h$ is shown for NNA receiver functions, whereas $P\delta_d\delta|_v$ is shown in the synthetics (since only SV signal is generated in 1-D modelling). Both the existence of SH signal in the real data and the fact that SH is better at resolving structure than SV are due to oblique illumination of the dipping structures and/or the presence of anisotropic discontinuities at Moho and 60 km depth. However, the fact that the polarity of the Moho and 60 km discontinuities keeps the same sign at all azimuths (*cf.*, Fig. 7) suggests that these may not be related to major anisotropic boundaries.

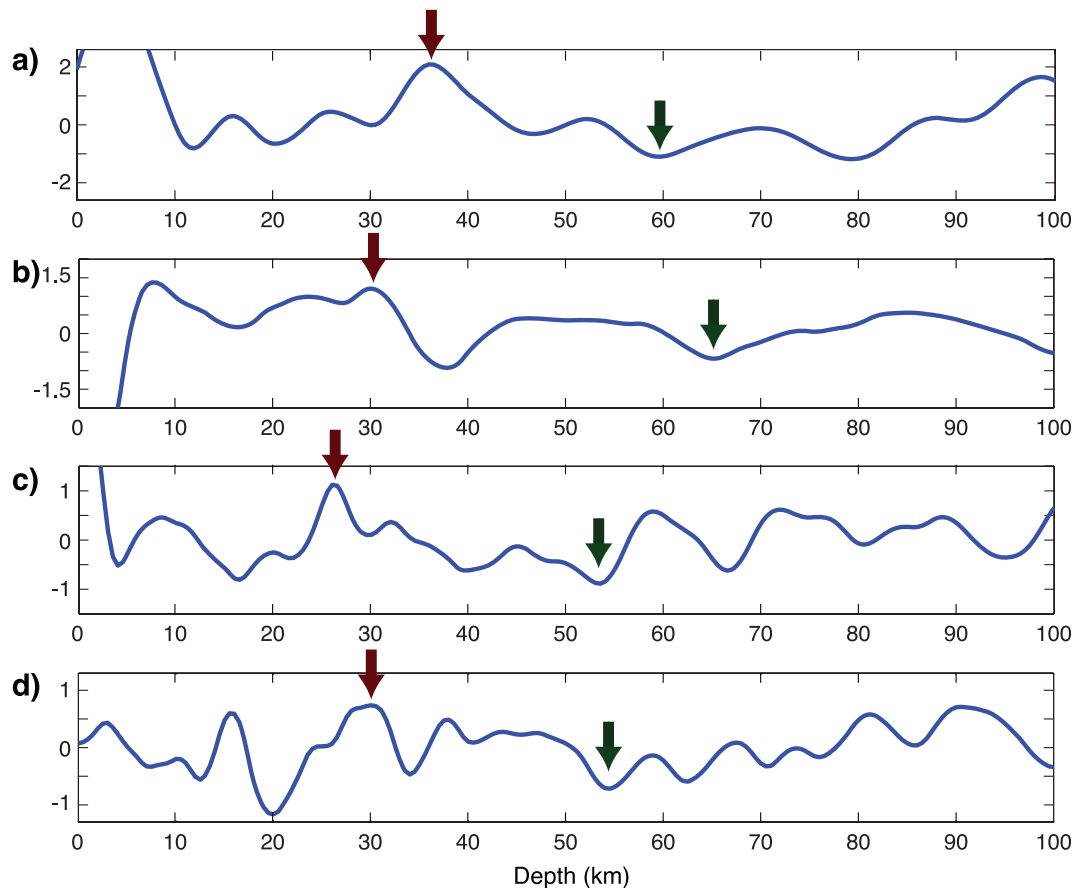


Figure 8. Stacked receiver functions obtained at station NNA from seven events with NW and SE backazimuths. Waveforms are migrated at 1-D phasing depths (i.e. conversion or reflection depths) corresponding to relevant forward and backscattered modes: (a) $P\delta\delta$, (b) $P\delta\delta p$, (c) $P\delta\delta$ (d) $P\delta\delta|h$. Tentative phase picks are denoted by arrows: red arrows indicate the phase corresponding to the Moho, whereas the green arrows point to the pulse of the 60 km discontinuity. Note that the two discontinuities appear at different depths in the various modes due to inaccuracies in the 1-D depth-migration operator used here; i.e. forward and backscattered waves sample subsurface discontinuities over lateral offsets that are likely marked by rapid fluctuations in discontinuity depth and Vp/Vs ratio (*cf.*, Section 3.3, see also Ai *et al.* 2005; Rossi *et al.* 2006), but map all these structures directly below the station. Although it does not take into account lateral Vp/Vs variations, the 2-D migration operator is better equipped to deal with variable azimuths and angles of illumination because it stacks phases at their conversion depth.

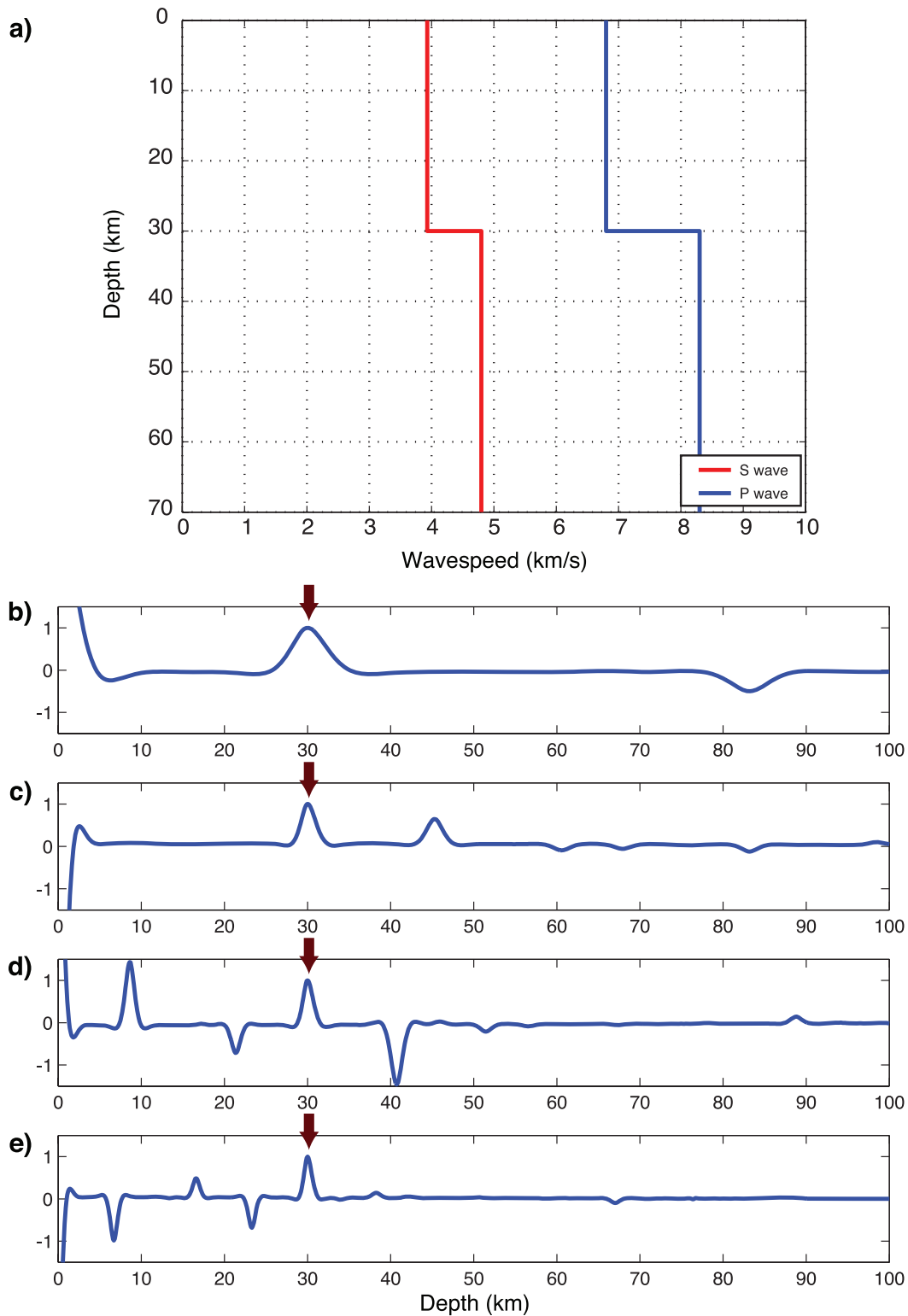


Figure 9. Synthetic receiver functions for a model with a single Moho discontinuity at 30 km depth, and an incident wave with horizontal slowness 0.05 s km^{-1} . (a) Synthetic model, (b) $P_d S$, (c) $P \dot{p}_d \dot{p}$, (d) $P \dot{p}_d S$ and (e) $P \dot{s}_d \dot{s}|_v$. Red arrows indicate the phase corresponding to the Moho. This model shows that a single discontinuity cannot explain the systematic occurrence in all modes of a negative phase near 60 km depth.

We can place approximate limits on the properties of the low-velocity layer either by using a rule of thumb based on the shortest wavelength λ in the recorded signal (e.g. Rychert *et al.* 2007), that is, maximum gradient thickness is $\lambda/2$ for transmission scattering and

$\lambda/4$ for reflection scattering, or by Ewald sphere analysis (Rondenay 2009). Given the highest frequency of 0.3 Hz, both methods suggest that the 60 km discontinuity is produced by an S -velocity anomaly of at least 10 per cent occurring over a gradient of at most 5 km. The

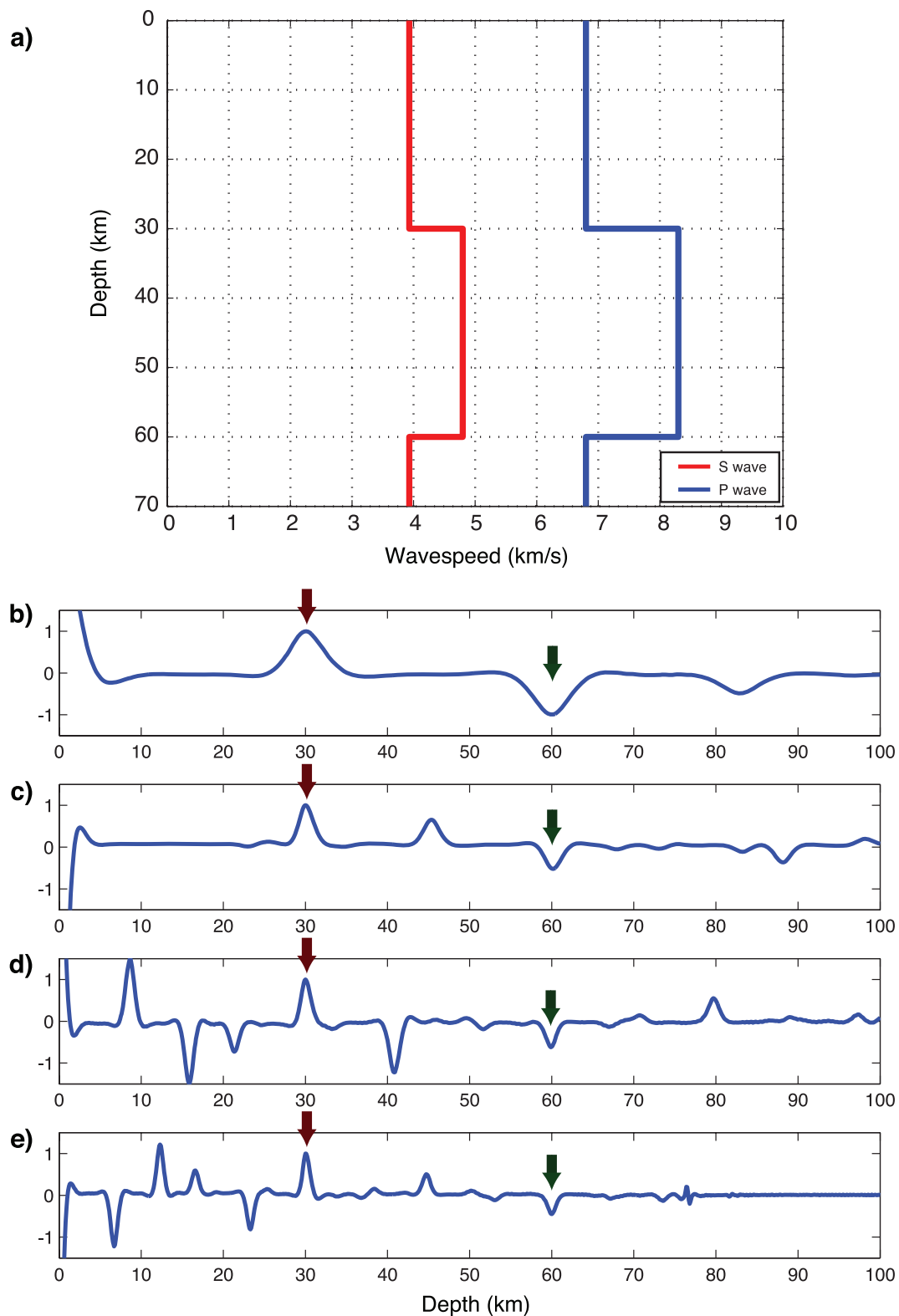


Figure 10. Synthetic receiver functions for a model with a single Moho discontinuity at 30 km depth, a negative velocity drop at 60 km depth, and an incident wave with horizontal slowness 0.05 s km^{-1} . (a) Synthetic model, (b) $P_d s_r$, (c) $P_p d_p$, (d) $P_p d_s$ and (e) $P_s d_s|_v$. Red arrows indicate the phase corresponding to the Moho, whereas the green arrows point to the pulse of the 60 km discontinuity. This is the only plausible model that can explain the systematic occurrence in all modes of a negative phase near 60 km depth.

fact that no consistent positive discontinuity is observed between 60 km and the top of the slab suggests one of two scenarios: either the velocities remain low throughout the mantle wedge, or the velocities return to normal mantle velocities over a smooth vertical gradient. For the latter scenario, resolution analysis indicate that velocities must return to average upper-mantle values over a gradient of at least ~ 10 km thickness. Thus, the low-velocity layer itself has a minimum thickness of 10 km.

4 INTERPRETATION OF THE SEISMIC RESULTS

4.1 Oceanic crust

The inference that the dipping low-velocity layer represents subducted oceanic crust is supported by refraction images obtained offshore of southern Alaska (Brocher *et al.* 1994). These profiles show that the oceanic crust that impinges on the trench is much thicker than regular oceanic crust, that is 18–20 km versus 10 km, respectively. Brocher *et al.* (1994) attribute this excess thickness to the superposition of the Yakutat terrane and the Pacific crust. Although our profile does not connect with the refraction transects, it is most probable that the low-velocity layer observed in our image is the extrapolation at depth of the composite Yakutat-Pacific crust observed at the trench (Ferris *et al.* 2003; Rondenay *et al.* 2008). Alternatively, the excess thickness of the low-velocity layer could be due to a serpentinized sliver of the mantle wedge directly above the subduction interface (Kawakatsu & Watada 2007), or a layer of serpentinized mantle beneath the subducted oceanic Moho (Ferris *et al.* 2003). However, as pointed out by Rondenay *et al.* (2008), there is no obvious reason why a deep serpentinized layer should be equal in thickness to the oceanic crust entering the trench.

The low-velocities progressively disappear in the upper part of the LVL, starting at 50 km, and terminates completely at ~ 120 km. In a previous paper, Rondenay *et al.* (2008) showed that this disappearance is a robust feature, and that it occurs at a depth where petrological and geodynamic models predict that the plate undergoes extensive dehydration and eclogitization, thus conferring high-velocities to the crust.

4.2 60 km discontinuity

The 60 km discontinuity is an unusual feature. To the best of our knowledge, no other seismic image of subduction zone has documented the existence of such sharp boundary in the middle of the mantle wedge (e.g. Yuan *et al.* 2000; Rondenay *et al.* 2001; Nicholson *et al.* 2005; Kawakatsu & Watada 2007; Suckale *et al.* 2009). It is therefore reasonable to state that this feature is, if not unique, at least rare and that its occurrence beneath central Alaska is due to the peculiar dynamics of this subduction system.

The 60 km discontinuity represents a negative seismic velocity gradient of 10–13 per cent over <10 km (based on the highest frequency at which it is detected). Candidate causes for such a discontinuity are thermal boundaries and compositional boundaries. The former is, however, an unlikely explanation as a 10–13 per cent velocity contrast at 60 km depth requires a localized thermal gradient of >400 °C over ~ 10 km, which is greater and much sharper than the continuous $10\text{--}20$ °C km⁻¹ gradient predicted by steady-state geodynamic models (Section 5.2; see also, e.g. Rondenay *et al.* 2008). However, if the 60 km discontinuity marks the top of a low-velocity layer, the base of this layer may be due to such a smooth

temperature gradient since it is not detected by converted seismic waves.

Compositional boundaries involve transitions in chemical and/or physical properties of wedge material. Chemical layering is supported here by recent receiver function results indicating an anomalously low Poisson's ratio <1.7 in the upper 20–30 km of the mantle wedge (Rossi *et al.* 2006). However, the common form of chemical variation involving iron-depletion accounts for at most 1 per cent velocity perturbation (Schutt & Leshner 2006), well under the velocity reduction observed here. Other possible compositional transitions include a boundary between dry lithosphere and hydrated asthenosphere/mantle wedge, which can account for up to ~ 4 per cent perturbation (considering attenuation effects of water in nominally anhydrous mantle minerals; see, e.g. Rychert *et al.* 2007). Alternatively, mixing of crustal rocks in the mantle wedge through tectonic processes (Rossi *et al.* 2006) or diapirism (Gerya & Yuen 2003) may produce higher velocity contrasts similar to those observed at 60 km depth.

A transition in physical properties, such as that from a solid layer above to a layer containing partial melt or aqueous fluids below, may also be invoked. Partial melt could easily cause the observed S velocity contrast of $\sim 10\text{--}13$ per cent through anelastic loss, but the required melt fraction is difficult to determine given the wide range of values inferred from different experimental results (i.e. from $\ll 1$ per cent to several percent depending upon melt/fluid topology; see, e.g. Gribb & Cooper 2000; Takei 2002; Faul *et al.* 2004). Regardless of the exact melt fraction required, the 60 km discontinuity is therefore reminiscent of the lithosphere–asthenosphere boundary observed in other tectonic environments (Rychert *et al.* 2005).

Based on the geophysical constraints from results presented here and in previous studies of central Alaska, we cannot readily discriminate between several potential causes (i.e. composition, hydration, partial melt and fluids) for the 60 km discontinuity. Thus we recognize that the discontinuity could stem from any of these effects, either individually (except for hydration) or in combination. However, in the context of this study, we will assume that the discontinuity is mainly due to a horizon of ponded partial melt. This model is adopted because we can show that such a horizon is a natural consequence of the shallow subduction regime in central Alaska, and that it can explain the absence of volcanism in the Denali region.

5 ORIGIN OF THE DENALI VOLCANIC GAP

The segment of the Alaska-Aleutian subduction system sampled by the BEAAR experiment exhibits several unusual features. First, it lacks the volcanic activity usually found in subduction zones. Second, the thickness of the subducted crust (which includes the Yakutat terrane) is twice that of normal oceanic crust. Third, the subduction angle is shallow (22°) compared to the angle observed over the rest of the system ($40\text{--}50^\circ$) to the west of the volcanic gap. Fourth, our seismic results identify a discontinuity at 60 km depth that may be due to a layer of partial melt and/or fluids in the mantle wedge. Such a discontinuity is not seen at other subduction zones where volcanism is more robust (e.g. Rondenay *et al.* 2001; Nicholson *et al.* 2005; Kawakatsu & Watada 2007).

In this section, we present a new model in which shallow subduction of the buoyant Yakutat terrane alters the dynamic equilibrium of the mantle wedge and causes volcanic activity to shut down. In most subduction zones, mantle wedge circulation develops a hot, weak core and comprises an upward component of flow that reduces

the thermal thickness of the overriding lithosphere (van Keken *et al.* 2002; Kelemen *et al.* 2004). In the Denali region, we propose that the slab advances landward, replacing the hot core of the mantle wedge as it progresses. This reduces the intensity of mantle wedge circulation, thereby cooling the system, and flattens the base of the thermal lithosphere, thereby decreasing the ability of the system to focus melt and form an arc. We present modelling experiments showing that this slab advance alters the production and extraction of melt, resulting in the cessation of volcanic activity at the surface.

5.1 Requirements for melt production and extraction

Our proposed model is rooted in the requirements for the generation and extraction of hydrous magma, a fundamental product of the subduction factory (e.g. Tatsumi *et al.* 1983; Grove *et al.* 2009). Wet melting and arc volcanism hinge on the following physical and chemical conditions: (1) a source of water at depth, (2) sufficiently high temperatures that exceed the wet solidus of mantle peridotites and (3) a flow regime and wedge structure that allow efficient melt production and mechanical extraction through the lithosphere.

There is evidence that the first two conditions are met in southern Alaska. First, the presence of a water source in the mantle wedge is supported by the progressive thinning and eventual disappearance with depth of the dipping, low-velocity layer (Rondenay *et al.* 2008). Second, geophysical studies including thermal models (Abers *et al.* 2006; Rondenay *et al.* 2008) and evidence for low Q (Stachnik *et al.* 2004) predict temperatures $> 1000^\circ\text{C}$ in this part of the mantle wedge, in excess of the wet-solidus of peridotite for these depths ($\sim 900^\circ$, Grove *et al.* 2006). Thus, wet melt is likely generated in the mantle wedge beneath the Denali region, as confirmed by the occurrence of infrequent volcanic eruptions (Nye 1999). However, we believe that the third condition is not met.

Next, we describe numerical models of mantle circulation and temperature structure in subduction zones. To start, we present models of the mantle wedge for steady subduction, that is, without slab rollback or advance, which predict the development of a volcanic arc in the Denali region. Then, we show that an advancing slab, as is likely present beneath the Denali Volcanic Gap, may perturb mantle wedge circulation in a way that causes melt to pool at depth (causing the observed 60 km discontinuity) rather than erupt at the surface.

5.2 Thermal modelling: steady subduction

Thermal models of steady subduction systems (i.e. without slab advance or rollback) that consider temperature-dependent viscosity develop a hot core and a vaulted zone at the apex of the mantle wedge. Both features are due to upward flow of warm mantle material and associated erosion at the base of the overriding plate (see, e.g. van Keken *et al.* 2002; Kelemen *et al.* 2004). Following Kincaid & Griffiths (2004), we refer to the vaulted zone as the ‘pinch zone’ (see, also, Hsui *et al.* 1983). As discussed below, this pinch zone may play an important role in the extraction of melt to the surface. We thus explore its properties in more details.

Fig. 11 displays the steady-state temperature structure of subduction zones for geometries corresponding to Western Alaska and the Denali volcanic gap. Here, we only summarize the most important characteristics of these models (a full description is given in the online Supporting Information). Mantle flow is driven by a kinematically defined subduction interface down to a depth of 300 or 200 km for the Western Alaska and Denali Volcanic Gap models, respectively, with partial coupling along the slab interface to 100 km depth. As in Rondenay *et al.* (2008), the overriding crust is 40 km thick and immobile. We impose a 90 mW m^{-2} geotherm on the continental side (Blackwell & Richards 2004) and an oceanic plate

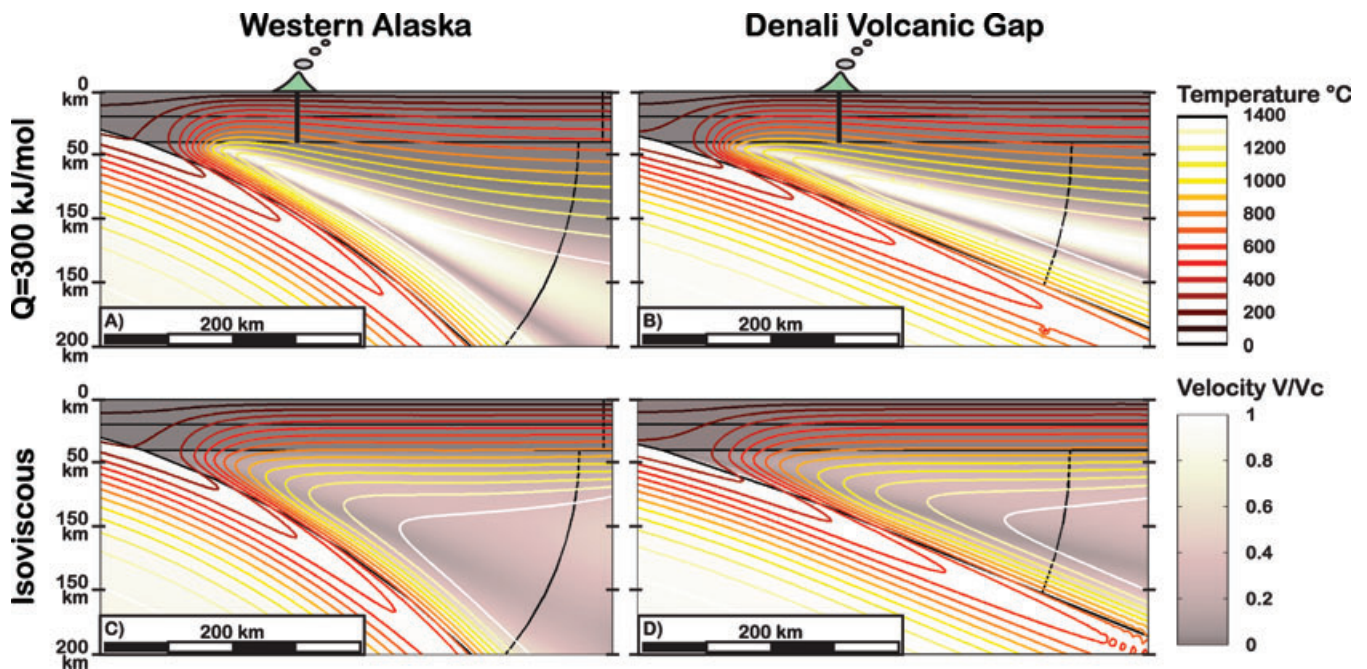


Figure 11. Steady-state thermal structure of a subduction zone following the geometry of Western Alaska (left-hand column) and the Denali Volcanic Gap area (right-hand column) for temperature-dependent viscosity (top row) and isoviscous (bottom row) models. The background field shows the intensity of the velocity. The volcano symbol marks the possible arc location. Each panel displays only a portion of a larger model described in the online Supporting Information.

cooling thermal profile on the oceanic side. The models are run to steady state without slab advance or rollback.

As a direct result of temperature-dependent viscosity, a strong pinch zone develops in the lithosphere of both subduction models shown in Fig. 11. The base of the crust exceeds 950°C in both the Western Alaska and Denali Volcanic Gap models, and the mantle wedge develops a hot core with temperature exceeding 1300°C underneath the pinch zone. Thus, these models predict abundant melt generation for subduction geometries corresponding to either western Alaska or the Denali volcanic gap. This implies that the Denali volcanic gap cannot be attributed solely to the shallow dip of the subducted slab below that region and suggests that the efficiency of melt extraction must be compromised.

5.3 Pinch zone and melt extraction

The mechanisms of melt focusing and extraction at plate boundaries are a topic of ongoing debate. Here, we choose to follow the melt propagation scenario proposed by Sparks & Parmentier (1991) for mid-ocean ridges. In the region of active melting, magma rises principally in a vertical direction regardless of the mantle flow field and its temperature. This is due to the buoyancy of the magma and the high permeability of partially molten systems (Faul 2001; Zhu & Hirth 2003). Eventually, the melt enters the cooler lithosphere, where it starts to crystallize. Provided that the crystallization rate is rapid enough, this process leads to the development of a low permeability zone, or permeability barrier (Korenaga & Kelemen 1997; Hebert & Montési 2009), under which magma accumulates to form a melt-rich zone (Sparks & Parmentier 1991; Spiegelman 1993; Katz 2008). There are no robust constraints on the P-T conditions at which such permeability barrier may occur in a subduction setting, but it likely follows an isotherm below the overriding crust. We can place a minimum bound at the upper ~850°C isotherm based on experimentally derived results for vapour-saturated melting (20 wt. per cent H₂O at 2 GPa; *cf.*, Grove *et al.* 2006). In contrast, magma composition analyses suggest that most arc magmas are generated at water undersaturated conditions and place an upper bound of ~1200°C for the temperature of the permeability barrier (see, e.g. Lee *et al.* 2009). If the permeability barrier is inclined, as is expected in the presence of a pinch zone (Fig. 11), melt flows along that barrier towards shallower depths like smoke under a roof. Melt is thus focused at the shallowest reaches of the permeability barrier in the pinch zone. Melt may also stall and accumulate where the permeability barrier reaches the base of the crust, because of the reduced density contrast between melt and the solid through which it travels. This accumulated melt may become pressurized; it eventually causes fracturing and erupts at the surface.

In the melt extraction scenario described above, the distributed melt and the melt-rich zone cause low-velocity and high attenuation anomalies that are observed seismically (Wiens & Smith 2003; Wiens *et al.* 2008). However, because melt migrates continuously, there may not be enough melt concentration along the permeability barrier to cause sharp discontinuities in material properties observable by converted/scattered seismic wave techniques—other than perhaps in the melt accumulation zone below the arc.

5.4 Thermal modelling: slab advance

The model of Fig. 11 (right-hand column) is not an accurate representation of the subduction regime beneath the Denali volcanic gap

because it ignores slab advance, which has taken place in that region probably since the Yakutat block entered the subduction system. We can include slab advance in our model by reducing the velocity of the downgoing plate and increasing correspondingly the velocity of the overriding plate.

The slab advance simulation is conducted in the reference frame of the subduction point, that is, the deepest point of contact between the overriding plate and the subducted slab. In this reference frame, the overriding plate moves at the trench migration velocity V_T towards the slab, and the subduction velocity imposed on the downgoing plate is $V_C - V_T$, where V_C is the observed convergence velocity.

Plate velocities may be estimated on the basis of the system's geometry and history. Slab contours imply that the slab has advanced by ~200 km in the Denali volcanic gap (Fig. 1). The timescale of this advance is poorly constrained, but we can place some bounds on it. On the one hand, slab advance may have taken place since the Yakutat terrane first entered the subduction system, *ca.* 12 Myr ago (e.g. Gulick *et al.* 2007), which would give a lower limit of $V_T/V_C = 0.30$. On the other hand, slab advance may have been initiated by the reported rapid change in plate convergence rate at 5.6 Ma (Fitzgerald *et al.* 1995), which would imply an upper limit of $V_T/V_C = 0.65$.

The slab advance model is integrated forward in time, with the initial conditions set to the reference structure of Fig. 11 (right-hand column). The results are presented in Fig. 12, which shows snapshots of the temperature field for $V_T/V_C = 0.25$ and 0.5. Although convergence between the plates remains unchanged in the slab advance model, the descent rate of the slab is slower than in the steady subduction regime. This progressively reduces the intensity of circulation in the wedge and, with it, the size of the pinch zone. In addition, as the slab advances towards the backarc domain, it takes the places of the hot core of the mantle wedge underneath the lithospheric pinch zone (Fig. 13). These processes lead to a shutdown of the intense circulation in the pinch zone and to a cooling of the mantle wedge.

In the Denali Volcanic Gap area, we are likely not in steady state yet, as this requires upward of 40 Myr (Fig. 12). However, it is clear from our modelling results that after as little as ~3 Myr of slab advance, the wedge has significantly cooled and the pinch zone is disappearing. This affects the melting regime in two important ways. First, the quantity of melt generated in the mantle wedge is strongly reduced both because temperatures are lower (see, e.g. Cagnioncle *et al.* 2007; Grove *et al.* 2009) and because the length of the melting column is shortened (Plank & Langmuir 1988). Second, the slope of the permeability barrier is strongly reduced (Fig. 12), causing whatever melt is generated in the wedge to no longer focus towards the pinch zone. Instead, it accumulates in the mantle beneath the crust. This model, in conjunction with our seismic observations, suggests that melt accumulation occurs in the vicinity of the 850°C isotherm at 60 km depth (compare Figs 4 and 12), which corresponds to the vapour-saturated solidus for that depth.

Our modelling results (including constraints on thermal behaviour and timescales) agree well with those of Arcay *et al.* (2008), who obtain a similar shallow subduction regime by considering upper plate advance towards the trench. These authors also show that such a regime causes upper plate compression in the region of the arc (see, also, Lallemand *et al.* 2005), as observed in our study area by the presence of the Chugach and Alaska ranges. We note that this compressive state further favours melt ponding, as it inhibits the opening of fractures in the overriding plate that would allow melt transport to the surface.

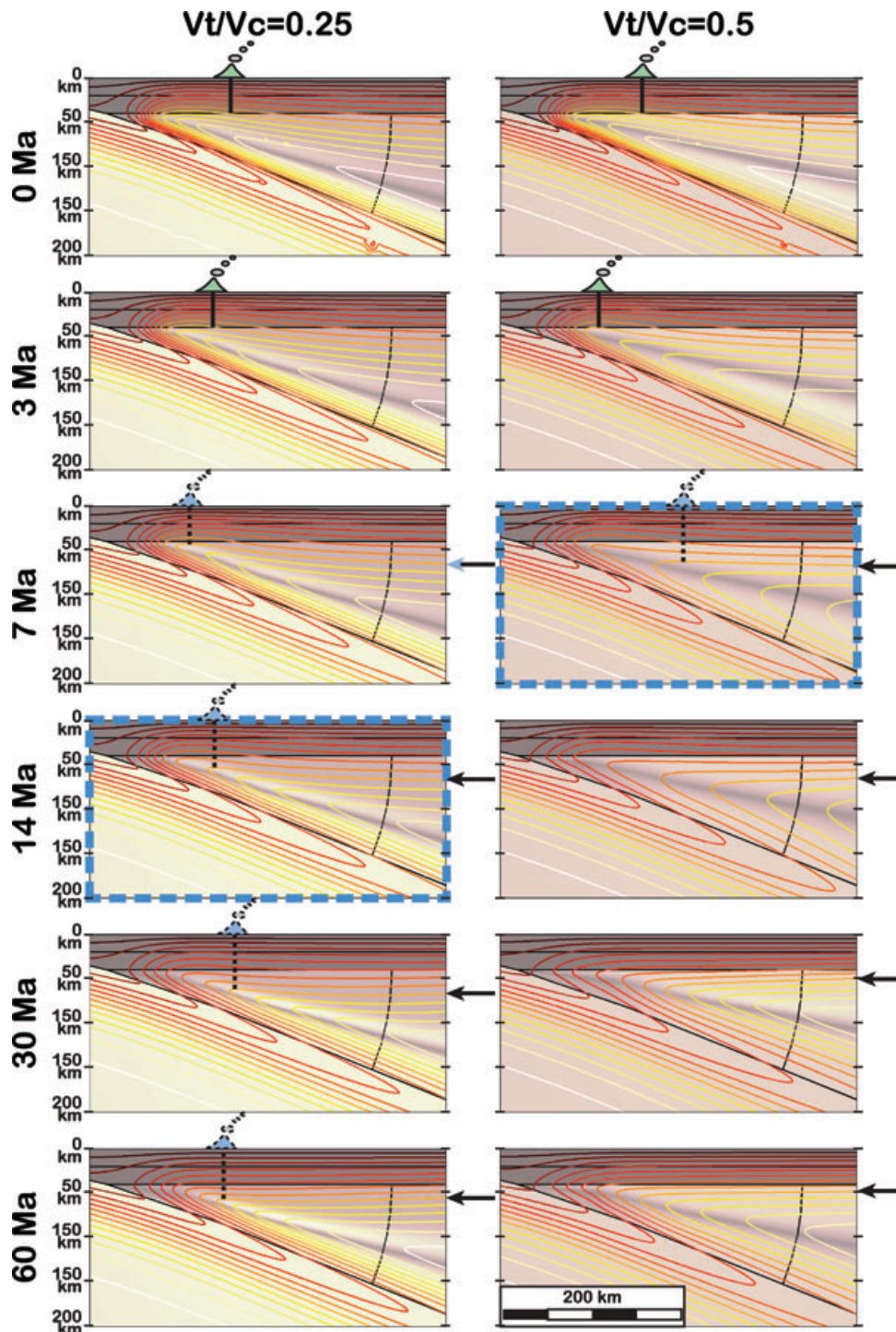


Figure 12. Time evolution of the temperature field of a subduction zone with slab geometry consistent with that of the Denali Volcanic Gap region, for slab advances at 25 per cent (left-hand column) or 50 per cent (right-hand column) of the convergence rate. The volcano symbol marks the possible arc location and the arrows point to the 900 °C isotherm (closest to the vapour-saturated solidus, at $\sim 850^\circ$ for 2GPa; see Grove *et al.* 2006). The highlighted models correspond to the current configuration of the wedge if slab advance started 14 or 7 My ago—i.e. accounting for ~ 200 km advance and a constant convergence rate of 55 mm yr^{-1} . Legend as for Fig. 11.

5.5 Applicability to other subduction zones

The absence of volcanism in the Denali region can be explained as a consequence of slab advance: low temperatures cause reduced melt production, melt pooling along a permeability barrier cause inefficient melt extraction, and the combination of these two phenomena

causes volcanism to shut down. Fig. 13 presents a summary diagram of our interpretation of mantle dynamics and seismic images in the Denali Volcanic Gap. This model differs from the mechanism invoked to explain volcanic gaps in the Andes. There, shallow subduction is thought to cause the cessation of volcanism by completely suppressing corner flow or dehydrating the slab before it meets the

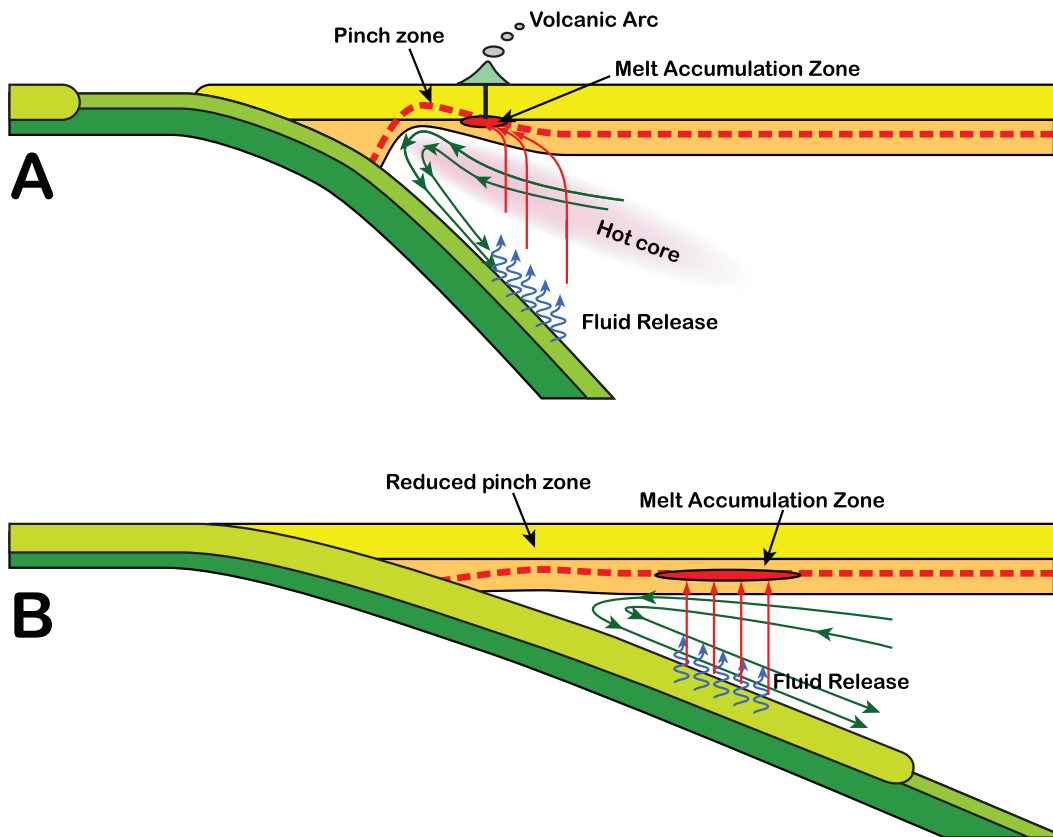


Figure 13. Schematic diagram summarizing the difference between (a) a reference steady subduction and (b) a subduction perturbed by slab advance. The subducting plate is colored in shades of green and the overriding plate in orange. The base of the overriding plate reflects a mechanical and/or thermal boundary. Circulation in the mantle is depicted by green arrows, fluxing of water into the mantle by blue arrows, and the trajectory of partial melts by red arrows. Steady subduction features a hot, low viscosity core with associated thermal erosion of the lithosphere, forming a ‘pinch zone’. Melts are assumed to travel upward to a permeability barrier (thick dashed red line), then along it towards the pinch zone. Melt accumulates either at the base of the crust (a) or where the permeability barrier is flat (b). Arc volcanism, indicated by the volcano and conduit symbol, most likely occurs when melt is focused towards the pinch zone at shallow depth. It is thus expected only for steady subduction (a) or slab rollback (Kincaid & Griffiths 2004). Slab advance (b) cools the mantle wedge, reducing melt production and flattening the permeability barrier, and causing the melt to accumulate at depth rather than erupt at the surface.

active portion of the mantle wedge (Kay *et al.* 1999). In contrast, our new seismic results show that most conditions necessary for producing melt exist below the Denali volcanic gap. However, shallow subduction causes the slab to advance, thereby inhibiting melt production and extraction by perturbing the thermal balance at the base of the lithosphere. Arc volcanism is therefore an indicator of the transient thermal environment in the mantle wedge: volcanism is invigorated when the subducted plate is in retreat (Kincaid & Griffiths 2004) and may shut down when the subduction front advances as is the case in the Denali region.

6 CONCLUDING REMARKS

The new, high-resolution seismic image of the central Alaska subduction zone presented in this paper outlines the abnormally thick crust of the Yakutat terrane subducting to 120 km depth, and a previously unidentified negative seismic discontinuity at 60 km depth. The subducted crust is observed as a thick, NW-dipping low-velocity layer between 50 and 120 km depth. Its termination is consistent with the depth where petrological and geodynamic models predict that the plate undergoes extensive dehydration and eclogitization, as previously shown in Rondenay *et al.* (2008). The 60 km discontinuity is possibly due to melt accumulation along an

undrained subhorizontal permeability barrier in the mantle wedge, and its presence in the mantle wedge of southern Alaska can explain the absence of volcanism in the Denali region. We formulate a thermally consistent model in which shallow subduction of the Yakutat terrane cools the system and causes the active portion of the mantle wedge to migrate landward, progressively engaging intact continental lithosphere from the backarc. The cooling reduces melt production and the disappearance of the pinch zone causes the melt to pond at the top of the mantle wedge, hindering magma extraction to the surface. This new model may help to further characterize the cessation of volcanism in other contemporary subduction zones (e.g. Kay *et al.* 1999), and to provide insight into arc volcanism during Archean times when shallow subduction is thought to have been more common (e.g. Bostock 1998).

ACKNOWLEDGMENTS

We thank the editor C. Thomas and two anonymous reviewers for their thoughtful suggestions, which helped improve the original manuscript. This work was supported by National Science Foundation grants EAR-0544996 (SR), EAR-0911151 (LGJM) and EAR-9996451 (GAA).

REFERENCES

- Abers, G.A., 2008. Orogenesis from subducting thick crust and evidence from Alaska, in *Active Tectonics and Seismic Potential of Alaska*, no. 179 in AGU Geophysical Monograph, pp. 337–349, eds Haeussler, P., Freymueller, J., Wesson, R. & Ekström, G., AGU, Washington, DC.
- Abers, G.A., van Keken, P., Kneller, E., Ferris, A. & Stachnik, J., 2006. The thermal structure of subduction zones constrained by seismic imaging: implications for slab dehydration and wedge flow, *Earth planet. Sci. Lett.*, **241**, 387–397.
- Ai, Y., Zhao, D., Gao, X. & Xu, W., 2005. The crust and upper mantle discontinuity structure beneath Alaska inferred from receiver functions, *Phys. Earth planet. Int.*, **150**, 339–350.
- Arcay, D., Lallemand, S. & Doin, M.-P., 2008. Back-arc strain in subduction zones: statistical observations versus numerical modeling, *Geochem. Geophys. Geosyst.*, **9**(5), Q05015, doi:10.1029/2007GC001875.
- Atwater, T., 1989. Plate tectonic history of the northeast Pacific and western North America, in *The Eastern Pacific Ocean and Hawaii, The Geology of North America*, pp. 21–72, eds Winterer, E.L., Hussong, D.M. & Decker, R.W., Geological Society of America, Boulder, Colorado.
- Blackwell, D.D. & Richards, M., 2004. Geothermal Map of North America, p. 1 sheet, Am. Assoc. Pet. Geol.
- Blakely, R.J., Brocher, T.M. & Wells, R.E., 2005. Subduction-zone magnetic anomalies and implications for hydrated forearc mantle, *Geology*, **33**(6), 445–448.
- Bostock, M.G., 1998. Mantle stratigraphy and evolution of the Slave province, *J. geophys. Res.*, **103**(B9), 21183–21200.
- Bostock, M.G. & Rondenay, S., 1999. Migration of scattered teleseismic body waves, *Geophys. J. Int.*, **137**, 732–746.
- Bostock, M.G., Rondenay, S. & Shragge, J., 2001. Multiparameter two-dimensional inversion of scattered teleseismic body waves, 1, Theory for oblique incidence, *J. geophys. Res.*, **106**, 30 771–30 782.
- Brocher, T., Fuis, G., Fisher, M., Plafker, G. & Moses, M., 1994. Mapping the megathrust beneath the northern Gulf of Alaska using wide-angle seismic data, *J. geophys. Res.*, **99**(B6), 11 663–11 685.
- Cagnioncle, A.-M., Parmentier, E.M. & Elkins-Tanton, L.T., 2007. Effect of solid flow above a subducting slab on water distribution and melting at convergent plate boundaries, *J. geophys. Res.*, **112**, B09402, doi:10.1029/2007JB004934.
- Conder, J., Wiens, D. & Morris, J., 2002. On the decompression melting structure at volcanic arcs and back-arc spreading centers, *Geophys. Res. Lett.*, **29**(15), 1727, doi:10.1029/2002GL015390.
- DeMets, C., Gordon, R.G., Argus, D.F. & Stein, S., 1994. Effect of recent revisions to the geomagnetic reversal time-scale on estimates of current plate motions, *Geophys. Res. Lett.*, **21**(20), 2191–2194.
- Eberhart-Phillips, D., Christensen, D.H., Brocher, T.M., Hansen, R., Ruppert, N.A., Haeussler, P.J. & Abers, G.A., 2006. Imaging the transition from Aleutian subduction to Yakutat collision in central Alaska, with local earthquakes and active source data, *J. geophys. Res.*, **111**, B11303, doi:10.1029/2005JB004240.
- Faul, U.H., 2001. Melt retention and segregation beneath mid-ocean ridges, *Nature*, **410**, 920–923, doi:10.1038/35073556.
- Faul, U.H., Gerald, J.D.F. & Jackson, I., 2004. Shear wave attenuation and dispersion in melt-bearing olivine polycrystals: 2. Microstructural interpretation and seismological implications, *J. geophys. Res.*, **109**, B06202, doi:10.1029/2003JB002407.
- Ferris, A., Abers, G.A., Christensen, D.H. & Veenstra, E., 2003. High resolution image of the subducted Pacific (?) plate beneath central Alaska, 50–150 km depth, *Earth planet. Sci. Lett.*, **214**, 575–588.
- Fitzgerald, P.G., Sorkhabi, R.B., Redfield, T.F. & Stump, E., 1995. Uplift and denudation of the central Alaska Range: a case study in the use of apatite fission track thermochronology to determine absolute uplift parameters, *J. geophys. Res.*, **100**(B10), 20 175–20 191.
- Fuis, G.S. *et al.*, 2008. Trans-Alaska Crustal Transect and continental evolution involving subduction underplating and synchronous foreland thrusting, *Geology*, **36**(3), 267–270, doi:10.1130/G24257A.1.
- Gerya, T. & Yuen, D., 2003. Rayleigh-Taylor instabilities from hydration and melting propel ‘cold plumes’ at subduction zones, *Earth planet. Sci. Lett.*, **212**, 47–62.
- Gribb, T.T. & Cooper, R.F., 2000. The effect of an equilibrated melt phase on the shear creep and attenuation behavior of polycrystalline olivine, *Geophys. Res. Lett.*, **27**(15), 2341–2344.
- Grove, T.L., Chatterjee, N., Parman, S.W. & Médard, E., 2006. The influence of H₂O on mantle wedge melting, *Earth planet. Sci. Lett.*, **249**, 74–89.
- Grove, T.L., Till, C.B., Lev, E., Chatterjee, N. & Médard, E., 2009. Kinematic variables and water transport control the formation and location of arc volcanoes, *Nature*, **459**, 694–697.
- Gulick, S., Lowe, L., Pavlis, T., Gardner, J. & Mayer, L., 2007. Geophysical insights into the Transition fault debate: propagating strike slip in response to stalling Yakutat block subduction in the Gulf of Alaska, *Geology*, **35**(8), 763–766.
- Gutscher, M.-A. & Peacock, S.M., 2003. Thermal models of flat subduction and the rupture zone of great subduction earthquakes, *J. geophys. Res.*, **108**(B1), 2009, doi:10.1029/2001JB000787.
- Hacker, B.R., Peacock, S.M., Abers, G.A. & Holloway, S.D., 2003. Subduction factory 2. Are intermediate-depth earthquakes in subducting slabs linked to metamorphic dehydration reactions? *J. geophys. Res.*, **108**(B1), 2030, doi:10.1029/2001JB001129.
- Hebert, L.B. & Montési, L.G., 2009. Melt permeability barriers beneath slow and ultra-slow mid-ocean ridges, *Geochim. cosmochim. Acta.*, **73**, A510.
- Hirschmann, M.M., 2000. Mantle solidus: experimental constraints and the effects of peridotite composition, *Geochem. Geophys. Geosyst.*, **1**, doi:10.1029/2000GC000070.
- Hsui, A., Marsh, B. & Toksöz, M., 1983. On melting of the subducted oceanic crust: effects of subduction induced mantle flow, *Tectonophysics*, **99**, 207–220.
- Hyndman, R.D. & Peacock, S.M., 2003. Serpentinization of the forearc mantle, *Earth planet. Sci. Lett.*, **212**, 417–432.
- James, D.E. & Sacks, I.S., 1999. Cenozoic formation of the central Andes: a geophysical perspective, in *Geology and Ore Deposits of the Central Andes*, Vol. 7 of Society of Economic Geologists Special Publication, pp. 1–25, ed. Skinner, B., Society of Economic Geologists, Littleton, CO.
- Katz, R.F., 2008. Magma dynamics with the enthalpy method: benchmark solutions and magmatic focusing at mid-ocean ridges, *J. Petrol.*, **49**(12), 2099–2121, doi:10.1093/petrology/egn058.
- Kawakatsu, H. & Watada, S., 2007. Seismic evidence for deep-water transportation in the mantle, *Science*, **316**, 1468–1471.
- Kay, S., Mpodozis, C. & Coira, B., 1999. Magmatism, tectonism, and mineral deposits of the central andes (22°–33°S), in *Geology and Ore Deposits of the Central Andes*, Vol. 7 of Society of Economic Geologists Special Publication, pp. 27–59, ed. Skinner, B., Society of Economic Geologists, Littleton, CO.
- Kelemen, P.B., Rilling, J.L., Parmentier, E.M., Mehl, L. & Hacker, B.R., 2004. Thermal structure due to solid-state flow in the mantle wedge beneath arcs, in *Inside the Subduction Factory*, Vol. 138 of AGU Geophysical Monograph, pp. 293–311, ed. Eiler, J.M., AGU, Washington, DC.
- Kincaid, C. & Griffiths, R., 2004. Variability in flow and temperatures within mantle subduction zones, *Geochem. Geophys. Geosyst.*, **5**, Q06002, doi:10.1029/2003GC000666.
- Kirby, S., Engdahl, E.R. & Denlinger, R., 1996. Intermediate-depth intraslab earthquakes and arc volcanism as physical expressions of crustal and uppermost mantle metamorphism in subducting slabs, in *Subduction Top to Bottom*, Vol. 96 of AGU Geophysical Monograph, pp. 195–214, eds Bebout, G., Scholl, D., Kirby, S. & Platt, J., AGU, Washington, DC.
- Korenaga, J. & Kelemen, P.B., 1997. Origin of gabbro sills in the Moho transition zone of the Oman ophiolite: implications for magma transport in the oceanic lower crust, *J. geophys. Res.*, **102**(B12), 27 729–27 749.
- Lallemand, S., Heuret, A. & Boutelier, D., 2005. On the relationships between slab dip, back-arc stress, upper plate absolute motion, and crustal nature in subduction zones, *Geochem. Geophys. Geosyst.*, **6**(9), Q09006, doi:10.1029/2005GC000917.

- Lee, C.-T.A., Luffi, P., Plank, T., Dalton, H. & Leeman, W.P., 2009. Constraints on the depths and temperatures of basaltic magma generation on Earth and other terrestrial planets using new thermobarometers for mafic magmas, *Earth planet. Sci. Lett.*, **279**, 20–33.
- Nicholson, T., Bostock, M. & Cassidy, J., 2005. New constraints on subduction zone structure in northern Cascadia, *Geophys. J. Int.*, **161**(3), 849–859.
- Nye, C., 1999. The Denali volcanic gap—magmatism at the eastern end of the Aleutian arc (abstract), *EOS, Trans. Am. geophys. Un.*, **80**(46), Fall Meet. Suppl., 1203, V52C–13.
- Page, R.A., Stephens, C.D. & Lahr, J.C., 1989. Seismicity of the Wrangell and Aleutian Wadati-Benioff zones and the North American plate along the Trans-Alaska crustal transect, Chugach mountains and Cooper River basin, southern Alaska, *J. geophys. Res.*, **94**, 16 059–16 082.
- Pavlis, T.L., Picornell, C., Serpa, L., Bruhn, R.L. & Plafker, G., 2004. Tectonic processes during oblique convergence: insights from the St. Elias Orogen, northern North American Cordillera, *Tectonics*, **23**, TC3001, doi:10.1029/2003TC001557.
- Plafker, G., Moore, J. & Winkler, G., 1994. Geology of the southern Alaska margin, in *The Geology of North America*, Vol. G-1: The geology of Alaska, pp. 389–449, eds Plafker, G. & Berg, H., Geol. Soc. Am., Boulder, CO.
- Plank, T. & Langmuir, C.H., 1988. An evaluation of the global variations in the major element chemistry of arc basalts, *Earth planet. Sci. Lett.*, **90**, 349–370.
- Ratchkovski, N. & Hansen, R., 2002. New evidence for segmentation of the Alaska subduction zone, *Bull. seism. Soc. Am.*, **92**, 1754–1765.
- Rondenay, S., 2009. Upper mantle imaging with array recordings of converted and scattered teleseismic waves, *Surv. Geophys.*, **30**, 377–405, doi:10.1007/s10712-009-9071-5.
- Rondenay, S., Bostock, M.G. & Shragge, J., 2001. Multiparameter two-dimensional inversion of scattered teleseismic body waves. 3: application to the Cascadia 1993 data set, *J. geophys. Res.*, **106**, 30 795–30 808.
- Rondenay, S., Bostock, M. & Fischer, K., 2005. Multichannel inversion of scattered teleseismic body waves: practical considerations and applicability, in *Seismic Earth: Array Analysis of Broadband Seismograms*, Vol. 157 of AGU Geophysical Monograph, pp. 187–204, eds Levander, A. & Nolet, G., AGU, Washington, DC.
- Rondenay, S., Abers, G.A. & van Keken, P.E., 2008. Seismic imaging of subduction zone metamorphism, *Geology*, **36**, 275–278.
- Rossi, G., Abers, G.A., Rondenay, S. & Christensen, D.H., 2006. Unusual mantle Poisson's ratio, subduction and crustal structure in central Alaska, *J. geophys. Res.*, **111**, B09311, doi:10.1029/2005JB003956.
- Rychert, C.A., Fischer, K.M. & Rondenay, S., 2005. A sharp lithosphere-asthenosphere boundary imaged beneath eastern North America, *Nature*, **436**, 542–545.
- Rychert, C.A., Rondenay, S. & Fischer, K.M., 2007. P-to-S and S-to-P imaging of a sharp lithosphere-asthenosphere boundary beneath eastern North America, *J. geophys. Res.*, **112**(B8), B08314, doi:10.1029/2007GL029535.
- Schutt, D. & Lesher, C., 2006. Effects of melt depletion on the density and seismic velocity of garnet and spinel lherzolite, *J. geophys. Res.*, **111**, B05401, doi:10.1029/2003JB002950.
- Shragge, J., Bostock, M. & Rondenay, S., 2001. Multiparameter two-dimensional inversion of scattered teleseismic body waves, 2, Numerical examples, *J. geophys. Res.*, **106**, 30 783–30 794.
- Sparks, D.W. & Parmentier, E.M., 1991. Melt extraction from the mantle beneath spreading centers, *Earth planet. Sci. Lett.*, **105**, 368–377.
- Spiegelman, M., 1993. Physics of melt extraction: theory, implications and applications, *Phil. Trans. Roy. Soc. Lond.*, **345**, 23–41.
- Stachnik, J., Abers, G. & Christensen, D., 2004. Seismic attenuation and mantle wedge temperatures in the Alaska subduction zone, *J. geophys. Res.*, **109**, B10304, doi:10.1029/2004JB003018.
- Suckale, J., Rondenay, S., Sachpazi, M., Charalampakis, M., Hosa, A. & Royden, L., 2009. High-resolution seismic imaging of the western Hellenic subduction zone using teleseismic scattered waves, *Geophys. J. Int.*, **178**(2), 775–791.
- Takei, Y., 2002. Effect of pore geometry on v_p/v_s : from equilibrium geometry to crack, *J. geophys. Res.*, **107**, 2043, doi:10.1029/2001JB000522.
- Tatsumi, Y., Sakuyama, M., Fukuyama, H. & Kushiro, I., 1983. Generation of arc basalt magmas and thermal structure of the mantle wedge in subduction zones, *J. geophys. Res.*, **88**(B7), 5815–5825.
- van Keken, P.E., Kiefer, B. & Peacock, S.M., 2002. High-resolution models of subduction zones: implications for mineral dehydration reactions and the transport of water into the deep mantle, *Geochem. Geophys. Geosyst.*, **3**(10), doi:10.1029/2001GC000256.
- Veenstra, E., Christensen, D., Abers, G. & Ferris, A., 2006. Crustal thickness variation in central Alaska: results from the Broadband Experiment Across the Alaska Range, *Geology*, **34**, 781–784.
- Wiens, D.A. & Smith, G.P., 2003. Seismological constraints on structure and flow patterns within the mantle wedge, in *Inside the Subduction Factory*, Vol. 138 of AGU Geophysical Monograph, pp. 59–82, ed. Eiler, J.M., AGU, Washington, DC.
- Wiens, D.A., Conder, J.A. & Faul, U.H., 2008. The seismic structure and dynamics of the mantle wedge, *Annu. Rev. Earth planet. Sci.*, **36**, 421–455.
- Yogodzinski, G., Lees, J., Churikova, T., Dorendorf, F., Wöerner, G. & Volynets, O., 2001. Geochemical evidence for the melting of subducting oceanic lithosphere at plate edges, *Nature*, **409**, 500–504.
- Yuan, X. *et al.*, 2000. Subduction and collision processes in the Central Andes constrained by converted seismic phases, *Nature*, **408**, 958–961.
- Zhao, D., Christensen, D. & Pulpan, H., 1995. Tomographic imaging of the Alaska subduction zone, *J. geophys. Res.*, **100**, 6487–6504.
- Zhu, W. & Hirth, G., 2003. A network model for permeability in partially molten rocks, *Earth planet. Sci. Lett.*, **202**, 407–416, doi:10.1016/S0012-821X(03)00264-4.

SUPPORTING INFORMATION

Additional Supporting Information may be found in the online version of this article:

Finite element models.

Table S1. Model parameters.

Figure S1. Example meshes for the Western Alaska model (A) and the Denali Volcanic Gap model (B, C). Geometry edges are highlighted in red and with nodes indicated by circles. The blue box in A and B delineates the wedge focus region shown in Figs 11 and 12 and in panel C. The coloured field represents the viscosity of the steady state subduction models using temperature-dependent viscosity with $Q = 300 \text{ kJ mol}^{-1}$ (as in Fig. 11). The maximum element size in the wedge region is 5 km in panels A and B and 2 km in panel C, as for the models of Figs 11 and 12.

Please note: Wiley-Blackwell are not responsible for the content or functionality of any supporting materials supplied by the authors. Any queries (other than missing material) should be directed to the corresponding author for the article.